This is the preprint of the contribution published as:

Zhu, B., Guo, R., Ye, Z., **Shao, H.**, Wang, L. (2026):
Quantitative assessment of field-scale natural gas hydrate production potential and efficiency via horizontal well depressurization
Energy Fuels **40** (14), 7350 - 7367

The publisher's version is available at:

https://doi.org/10.1021/acs.energyfuels.5c06477

Quantitative assessment of natural gas hydrate production potential and efficiency via horizontal well depressurization: modeling analysis based on hydrate-bearing sediments in the South China Sea

Bin Zhu [1, 2, 3], Ronghan Guo[1, 2, 3], Zhigang Ye[1, 2, 3, 4*], Haibing Shao[5], Lujun Wang[1, 2, 3]

[1] Institute of Hypergravity Science and Technology, Zhejiang University, Hangzhou 310058, China

[2] MOE Key Laboratory of Soft Soils and Geoenvironmental Engineering, Hangzhou, 310058, China.

[3] College of Civil Engineering and Architecture, Zhejiang University, Hangzhou, 310058, China.

[4] College of Civil Engineering and Architecture, Quzhou University, Quzhou, 324000, China.

[5] Department of Environmental Informatics, Helmholtz Centre for Environmental Research-UFZ, Permoserstr. 15, Leipzig, 04318, Germany

[*] Corresponding author: Zhigang Ye; E-mail: zhigangye@zju.edu.cn.

Abstract: Natural gas hydrates are widely recognized as a promising alternative to conventional fossil fuels. During depressurization, production efficiency gradually declines due to mass and heat transfer limitations within the maximum recoverable zone. This study integrates analytical solutions with numerical simulations to quantitatively evaluate production efficiency decline and identify high- and low-efficiency dissociation zones. Several indicators are proposed to characterize the effective production duration and the high-efficiency production zone in horizontal well depressurization. A stratified weighted average method is developed to extend the analytical model, enabling consideration of geothermal and pressure gradients as well as horizontal well configurations. By analyzing the mass and heat transfer characteristics of different reservoir types and well configuration strategies, optimal well configurations are recommended. The recoverable zone with enhanced permeability and the critical well length required for commercial production in the South China Sea hydrate reservoir are predicted. Results show that placing the horizontal well in the middle gas hydrate-bearing layer (GHBL) promotes long-term production and yields a higher gas water ratio. During hydrate exploitation through horizontal well depressurization, the recovery factor (R_{out}) varies slightly with permeability (0.18-0.21). However, with sufficient heat supplementation, R_{out} increases markedly and continues to rise with increasing permeability. Therefore, a combined strategy of permeability enhancement and heat injection is recommended for commercial exploitation. Energy return on investment (EROI) analysis indicates maximum economic efficiency when the GHBL permeability reaches 144 mD; however, considering fracturing costs, targeting permeability below this value is advisable. These findings provide theoretical guidance for optimizing gas hydrate production via depressurization.

Keywords: Hydrate-bearing sediments; Horizontal well depressurization; Recovery efficiency; Maximum recoverable gas; Quantitative analysis; South China Sea

1 Introduction

Natural gas hydrates (NGHs) are widely distributed in terrestrial permafrost and shallow submarine sediments (Sloan *et al.*, 2007). Characterized by high energy density and vast global reserves—estimated to exceed the total organic carbon of all proven fossil fuels—NGHs are recognized as a promising clean energy alternative to conventional petroleum and coal (Moridis *et al.*, 2011; Dong *et al.*, 2024). Among various exploitation technologies, depressurization is generally considered the most feasible for field-scale application due to its operational simplicity and low energy consumption (Li *et al.*, 2016). Field production tests in the Nankai Trough and the Shenhu area have validated the technical feasibility of this method, demonstrating that horizontal wells yield significantly higher productivity than vertical wells (Yamamoto *et al.*, 2014, 2019; Ye *et al.*, 2018, 2020; Moridis *et al.*, 2009; Feng *et al.*, 2019; Zhao *et al.*, 2023). Nevertheless, the achieved production levels remain well below the commercialization threshold for hydrate exploitation of 2.0×10^5 m^3/d (Wu *et al.*, 2021; Pang *et al.*, 2022; Wu *et al.*, 2022).

The production capacity of NGHs is largely constrained by the mass and heat transfer conditions within the reservoir. To enhance gas production efficiency, extensive studies have been carried out on reservoir type selection, exploitation scheme optimization (Li *et al.*, 2021; Lv *et al.*, 2022; Wei *et al.*, 2022; Cheng *et al.*, 2023; Ge *et al.*, 2023; Sun *et al.*, 2024; Qin *et al.*, 2025), and reservoir stimulation. Numerical simulations have revealed that coupled production from the hydrate layer and the underlying free gas layer (Wei *et al.*, 2022; Lv *et al.*, 2022; Cheng *et al.*, 2023) and optimized well configuration (Ge *et al.*, 2023) can significantly enhance productivity. Furthermore, commercial potential is verified through laboratory experiments and in-situ numerical simulations (Ye *et al.* 2025). Despite these optimizations, studies have indicated that commercial exploitation remains challenging in low-permeability reservoirs when relying solely on methods like depressurization or thermal stimulation (Yu *et al.*, 2021; Shang *et al.*, 2022). Emerging technologies such as microwave heating

(Fan *et al.*, 2025; Zhang *et al.*, 2026), novel gas injection methods (Kan *et al.*, 2025) and hydraulic fracturing have been explored to overcome these limitations. Regarding fracturing, the effect of fracture parameters, including permeability, spacing, length (Zhong *et al.*, 2021; Mao *et al.*, 2023; Zhang *et al.*, 2024; Li *et al.*, 2025), fracture dip (Sun *et al.*, 2019; Mu *et al.*, 2025), and morphology (Xu *et al.*, 2023) on gas production performance under horizontal well depressurization have been investigated. Furthermore, recent studies utilizing coupled geomechanical models have simulated the dynamic propagation process of fractures, revealing the complex interaction between fracture network evolution and hydrate dissociation (Huang *et al.*, 2024; Cheng *et al.*, 2025). In addition, combining reservoir stimulation with burden sealing has been proven effective to mitigate seawater intrusion. Numerical and field-based studies indicate that this integrated approach can significantly enhance gas recovery while controlling water production (Li *et al.*, 2021; Sun *et al.*, 2024; Qin *et al.*, 2025). In summary, previous studies on hydrate exploitation have mainly focused on gas production performance under single or multiple enhancement methods. However, the coupled mechanisms of hydrate dissociation with mass and heat transfer have received limited attention. Moreover, quantitative investigations into the effects of reservoir type and well configuration on production efficiency remain relatively insufficient.

From a mass transfer perspective, analytical solutions have been established to estimate the maximum recoverable zone and determine optimal well spacing for horizontal well systems (Terzariol *et al.*, 2017; Terzariol and Santamarina, 2021). To capture the time-dependent characteristics, semi-analytical Inflow Performance Relationship (IPR) models have been developed to forecast dynamic production rates (Lu *et al.*, 2018; Zhang *et al.*, 2022). While such approaches are effective for forecasting temporal production trends and total wellhead rates, they inherently prioritize the overall system performance over the spatial evolution of hydrate dissociation. As shown in Fig. 1, during the depressurization of NGHs, a large pressure drop and strong dissociation driving force occur in the near-wellbore zone, forming a high-efficiency

dissociation zone. In contrast, in zones far from the wellbore, the pressure drop transmission attenuates, heat supply becomes limited, and the hydrate dissociation rate decreases significantly (Yang *et al.*, 2016; Cheng *et al.*, 2024), forming a slow dissociation zone. After a sufficiently long period of exploitation, the seepage flow tends to stabilize, the temperature gradually returns to its initial state, and the hydrate dissociation boundary ceases to advance; this final zone is defined as the maximum recoverable zone. Establishing criteria for identifying the high-efficiency dissociation zone under different reservoir conditions is essential. Such criteria enable the quantitative evaluation for depressurization production efficiency, thereby improving the assessment of single-well production performance and the optimal design of enhancement measures. Currently, research focusing on the quantitative identification of these critical zones remains limited.

The evolution of gas production potential and production efficiency during hydrate depressurization is affected by multiple factors, including reservoir properties and reservoir types. However, existing studies lack a unified and effective evaluation method as well as a systematic quantitative analysis approach. This study extends the analytical solution for the maximum recoverable zone of horizontal well depressurization by incorporating evolution of productivity and complex field conditions. Evaluation indicators for high-efficiency production duration and high-efficiency production zone are proposed. The effects of geothermal and pressure gradients, well configuration, reservoir types, and reservoir properties are systematically investigated, and the validity of the proposed approach is verified through comparison with numerical simulations. This study analyzes the depressurization production of the hydrate reservoir in the Shenhu area of the South China Sea via numerical simulation, guided and verified by the analytical solutions. The enhancement effects under various permeability improvement conditions are evaluated, and the threshold conditions for achieving commercial exploitation are determined. This work provides a theoretical method for assessing the gas production

potential of a single horizontal well and offers important implications for hydrate development.

2 Methodology

Hydrate exploitation involves processes such as hydrate dissociation, skeleton deformation, gas-liquid migration, and heat transfer. The model is established under the following assumptions: (1) heat transfer occurs through both conduction and advection; (2) Darcy's law and Fick's law are applied to describe the seepage and diffusion of pore water and dry air, respectively; (3) hydrate dissociation rate is governed by the Kim-Bishnoi kinetic dissociation model, where no NGH secondary formation or ice formation occurs during the dissociation process (see Fig. C-1). Accordingly, the governing equations used are as follows:

2.1 Governing equations

2.1.1 Mass balance equations

Considering dissolved methane in liquid phase and water vapor in gas phase, the mass balance equations for methane and water are given as follows (Sanavia *et al.*, 2006; Teymouri *et al.*, 2020):

$$\frac{\mathrm{d_s}}{\mathrm{d}t}\sum_{\alpha=\mathrm{L,\,G}} N_\alpha \varphi_\alpha x_\alpha^c + \nabla\cdot\sum_{\alpha=\mathrm{L,\,G}}\left(N_\alpha x_\alpha^c \mathbf{q}_\alpha + N_\alpha \mathbf{J}_\alpha^c\right) + \sum_{\alpha=\mathrm{L,\,G}} N_\alpha \varphi_\alpha x_\alpha^c \nabla\cdot\frac{\mathrm{d_s}\mathbf{u}}{\mathrm{d}t} = \frac{q_c}{M_c} \quad (1)$$

where $\frac{\mathrm{d_s}}{\mathrm{d}t}$ is the material time derivative following the solid skeleton, α represents the liquid (L) or gas phase (G), c denotes water (w) or methane (m), N_α refers to the molar density of phase α, φ_α stands for the volumetric fraction of phase α, x_α^c is the component c molar fraction in phase α, $\mathbf{u}$ indicates the displacements, q_c signifies the source/sink term of component c, which can be determined by hydrate dissociation, and M_c represents the molar mass for component c. $\mathbf{q}_\alpha$ corresponds to the velocity of advective part for phase α, $\mathbf{J}_\alpha^c$ symbolizes the flux of diffusive part for phase α. $\mathbf{q}_\alpha$ follows Darcy's law and $\mathbf{J}_\alpha^c$ obeys Fick's law respectively:

$$\mathbf{q}_\alpha = -\frac{\mathbf{K}k_{r\alpha}}{\mu_\alpha}\left(\nabla p_\alpha - \rho_\alpha \mathbf{g}\right) \tag{2a}$$

$$\mathbf{J}_\alpha^c = -\frac{\varphi_\alpha}{\tau_\alpha}\mathbf{D}_\alpha^c \nabla x_\alpha^c \tag{2b}$$

where μ_α is the viscosity of phase α, $\mathbf{g}$ represents the gravity constant, $\mathbf{D}_\alpha^c$ stands for the diffusion coefficient of c in phase α, and p_α refers to the pore pressure of phase α. ρ_α signifies the density of phase α, τ_α symbolizes tortuosity of phase α.

2.1.2 Energy conservation equation

The local thermal equilibrium (LTE) assumption is adopted here, as low fluid velocities in unfractured porous media allow sufficient inter-phase heat exchange (Gamwo and Liu, 2010; Liao *et al.*, 2022), though its applicability typically excludes hydraulic fracturing or external heating scenarios (Shan *et al.*, 2024). Based on this LTE assumption, the total energy conservation over all phases is governed by (Sanavia *et al.*, 2006; Teymouri *et al.*, 2020):

$$\frac{\mathrm{d_s}}{\mathrm{d}t}\sum\nolimits_{\alpha=\mathrm{L,G,\,H,\,S}}\left(\rho_\alpha U_\alpha \varphi_\alpha\right) + \nabla\cdot\mathbf{J}_\mathrm{c} + \nabla\cdot\sum\nolimits_{\alpha=\mathrm{L,G}}\left(\rho_\alpha H_\alpha \mathbf{q}_\alpha\right) = q_\mathrm{E} \tag{3}$$

where U_α is the specific internal energy for phase α, H_α refers to the specific enthalpy energy for phase α, q_E represents the energy source/sink term, which can be calculated by hydrate dissociation, and $\mathbf{J}_\mathrm{c}$ indicates the heat conduction flux, which is usually described by Fourier's law:

$$\mathbf{J}_\mathrm{c} = -\mathbf{k}_T \nabla T \tag{4}$$

where $\mathbf{k}_T$ is the equivalent heat conductive coefficient, usually formulated as $\mathbf{k}_T = \mathbf{k}_{T\mathrm{dry}} + \left(\sqrt{s_\mathrm{L}} + \sqrt{s_\mathrm{H}}\right)\left(\mathbf{k}_{T\mathrm{sat}} - \mathbf{k}_{T\mathrm{dry}}\right)$ (White *et al.*, 2020).

2.1.3 Momentum balance equation

Neglecting the inertial forces, the linear momentum equation considering gravity for all phases reads as follows (Sanavia *et al.*, 2006; Teymouri *et al.*, 2020):

$$\nabla\cdot\left(\boldsymbol{\sigma}' - \frac{S_\mathrm{L}p_\mathrm{L} + S_\mathrm{G}p_\mathrm{G}}{S_\mathrm{L}+S_\mathrm{G}}\mathbf{1}\right) + \sum\nolimits_{\alpha=\mathrm{L,G,\,H,\,S}}\left(\rho_\alpha \varphi_\alpha\right)\mathbf{g} = \mathbf{0} \tag{5}$$

where ∇ is the Nabla operator, $\boldsymbol{\sigma}'$ represents the effective stress tensor, which can be expressed as:

$$\boldsymbol{\sigma}' = \mathbf{D^e}:(\boldsymbol{\varepsilon} - \boldsymbol{\varepsilon}_T) = \mathbf{D^e}:\frac{\nabla\mathbf{u}+\nabla^{\mathrm{T}}\mathbf{u}}{2} - \mathbf{D^e}:\mathbf{1}\frac{\beta_{\mathrm{s}}}{3}(T - \mathrm{T}_0) \quad (6)$$

where $\mathbf{1}$ is the second-order identity tensor, $\mathbf{D^e}$ denotes the elasticity tensor, $\boldsymbol{\varepsilon}$ indicates the total strain tensor, $\boldsymbol{\varepsilon}_T$ is the thermal strain tensor, β_{s} symbolizes the volumetric thermal expansion coefficient of solid phase, T_0 represents the initial temperature.

2.1.4 Gas hydrate kinetic model

There are several dissociation models based on pure hydrates, including the equilibrium equation (Kowalsky and Moridis, 2007), the quasi-kinetic equation (Sánchez *et al.*, 2018), and the kinetic dissociation equation (Kim *et al.*, 1987). Among these, the Kim-Bishnoi kinetic dissociation model is widely recognized and frequently employed for characterizing the kinetic reaction process of hydrates:

$$R_{\mathrm{r}} = -K_0 \exp\left(\frac{\Delta E}{RT}\right) A_{\mathrm{s}}(p_{\mathrm{e}} - p_{\mathrm{G}}) \quad (7a)$$

$$p_{\mathrm{e}} = -c_{\mathrm{E}} \exp\left(a_{\mathrm{E}} T^{b_{\mathrm{E}}}\right) \quad (7b)$$

$$A_{\mathrm{s}} = A_{\mathrm{s0}} \varphi S_{\mathrm{H}} \quad (7c)$$

where R_{r} is the amount of substance of hydrates per unit volume, K_0 indicates intrinsic kinetic dissociation constant, ΔE represents the activation energy, R refers to the ideal gas constant, T denotes temperature, p_{e} is equilibrium pressure, a_{E}, b_{E}, and c_{E} signifies the coefficients related to equilibrium pressure, A_{s} stands for the specific surface area of dissociation, A_{s0} denotes the initial specific surface area of dissociation, φ is porosity, and s_{H} represents hydrate saturation.

Based on the aforementioned equations, a multi-field coupling model for hydrate exploitation has been established and solved using the OGS-Hydrate numerical model developed by Ye *et al.* (2022) based on the open-source finite element software OpenGeoSys (Kolditz *et al.*, 2012; Bilke *et al.*, 2019). The key procedure is as follows (Ye *et al.*, 2022, 2023): (1) the hydrate kinetic reaction equation is used to solve for the hydrate reaction rate, obtaining the rates of gas production, water production, and heat absorption, which are then coupled with the source/sink terms for mass and energy; (2) in the local, the Nonlinear Complementarity Problem (NCP) method is introduced to

accurately solve the process of gas-liquid phase appearance and disappearance. The reliability of this coupling strategy has been rigorously verified against the numerical benchmark for the THM process (Schrefler *et al.*, 1995) and the experimental data of NGH dissociation (Masuda *et al.*, 1999) in the previous studies (Ye *et al.*, 2022). In the global, the Domain Decomposition Method (DDM) is employed to achieve high-performance parallel computing. Furthermore, systematic uncertainty analyses based on the second international gas hydrate code comparison study (IGHCCS2) benchmark demonstrate that the long-term production behavior is robust against variations in thermal conductivity and intrinsic dissociation rates (See Fig. C-2 in Appendix C). Meanwhile, pore water compressibility is strictly accounted for in the coupled simulations to accurately confine the spatial extent of reservoir deformation (Ye *et al.*, 2023).

2.2 Production assessment via horizontal well depressurization

2.2.1 Maximum recoverable zone of a horizontal well

During NGH depressurization-based exploitation, the gas-liquid seepage gradually reaches a steady state. Once the hydrate dissociation boundary ceases to expand, the maximum recoverable zone is reached. This zone determines the recoverable gas, and affects the production efficiency and ultimate gas recovery. Terzariol *et al.* (2017) derived an analytical solution for the maximum recoverable zone under single horizontal well depressurization, expressed as follows (the detailed derivation is provided in Appendix A):

$$\frac{\left[2\left(\frac{P_{\mathrm{far}}-P_{\mathrm{w}}}{P_{\mathrm{far}}-P_{\mathrm{e}}}\right)e^{\left(\frac{r_{\mathrm{w}}-x^{*}}{\lambda_{\mathrm{sed}}}\right)}-e^{\left(-2\frac{x^{*}-r_{\mathrm{w}}}{\lambda_{\mathrm{sed}}}\right)}-1\right]}{1-e^{\left(-2\frac{x^{*}-r_{\mathrm{w}}}{\lambda_{\mathrm{sed}}}\right)}}=\sqrt{\frac{k_{\mathrm{hbs}}}{k_{\mathrm{sed}}}} \tag{8}$$

where P_{far} is the fluid pressure in the far field, P_{w} represents the fluid pressure at the well, P_{e} refers to the fluid pressure at the phase boundary, k_{sed} stands for sediment permeability without hydrates, k_{hbs} indicates the hydrate-bearing sediment permeability, $k^{'}$ symbolizes the burden permeability, x^{*} denotes the terminal hydrate dissociation

boundary distance, i.e., the maximum recoverable zone, *b* corresponds to the burden thickness, *H* is the gas hydrate-bearing layer (GHBL) thickness, λ_{sed} is the characteristic length, usually formulated as $\lambda_{\mathrm{sed}} = \sqrt{k_{\mathrm{sed}} Hb \,/\, 2k'}$.

2.2.2 Analytical extension for reservoir gradients and well configuration

The assumptions of the aforementioned analytical solution for the maximum recoverable zone deviate from actual reservoir conditions. In actual reservoirs, the properties of the overburden (OB) and underburden (UB) are often different; the geothermal gradient and gravity cause non-uniform distribution of geothermal and pressure in the reservoir; furthermore, the horizontal well may not be located at the center of the GHBL. Aiming to better reflect the influence of these actual conditions, this study introduces a stratified weighted average method to further extend the application scope of the above analytical solution. Under this framework, the maximum recoverable zone can be defined as:

$$x^* = \frac{x^*_{\mathrm{up}} w_{\mathrm{up}} + x^*_{\mathrm{down}} w_{\mathrm{down}}}{w_{\mathrm{up}} + w_{\mathrm{down}}} \tag{9a}$$

$$w_i = 1 - \frac{n_{\mathrm{m}i}}{\sum_{i=\mathrm{up,down}} n_{\mathrm{m}i}} \tag{9b}$$

where x^* denotes the analytically predicted maximum recoverable zone, *w* stands for the weight of natural gas reserves, *n* is the molar amount of natural gas in the corresponding zone, the subscript up represents the upper part of the reservoir, the subscript down indicates the lower part of the reservoir, the subscript m is natural gas, the subscript *i* symbolizes different parts of the reservoir (*i* stands for up or down). The validation of this method and the detailed discussion regarding these influences will be presented in Section 3.2.

2.2.3 High-efficiency production duration/Evaluation metric for production efficiency

During the depressurization exploitation of NGHs, the gas production efficiency gradually decays over time. Therefore, accurately evaluating the high-efficiency production duration is of great significance for optimizing production schemes and

improving overall recovery performance. In this study, the analytical solution is employed to determine the recoverable methane gas reserves in a system involving a horizontal well. The ratio of cumulative gas production to these recoverable reserves is defined as the recovery factor, serving as an indicator of the efficiency of the depressurization process:

$$R_{\mathrm{out}} = \frac{V_{\mathrm{p}}}{V_{\mathrm{Total}}} \tag{10}$$

where R_{out} is the recovery factor, V_{P} represents the cumulative gas production, V_{Total} refers to the recoverable methane gas reserves, obtained from Equation (8). By dynamically tracking the evolution of R_{out} during the numerical simulations, a specific threshold can be identified to demarcate the high-efficiency production stage. The detailed determination of this duration and the corresponding dynamic behavior of R_{out} will be discussed in Section 3.3.

2.3 Numerical model

The second hydrate production test of China in 2020 is located on the northern continental slope of the Baiyun Sag in Pearl River Mouth Basin, South China Sea. Logging data from well GMGS6-SH02 reveal that the region consists of an overburden (OB), a gas hydrate bearing layer (GHBL), a three-phase layer (TPL), a free gas layer (FGL), and an underburden (UB) (Ye *et al.*, 2020). To investigate the effects of reservoir types on depressurization performance, numerical models were developed for three representative reservoir types (Wang *et al.*, 2023) and the second production test case. The reservoir schematics and horizontal well configurations for these models are illustrated in Fig. 2.

The Class I, Class II and Class III reservoir models measure 149.2 m × 100 m. Among them, the GHBL has a thickness of 70.2 m, the FGL/FWL is 19 m thick. The horizontal wells are positioned 17.55 m, 35.1 m, and 52.65 m below the top of the GHBL, denoted by the subscripts upper, middle, and lower, respectively. The second

production test reservoir model measures 149.2 m × 600 m. The horizontal well length is 280 m, located in the middle of the TPL and the GHBL. The top and bottom boundaries of the model are constant temperature and constant pressure boundaries, where the top boundary temperature is 283.58 K and pressure is 14.10 MPa, the pressure gradient is hydrostatic, and the thermal gradient is 0.0443 K/m. Depressurization is conducted in two stages: (1) uniform pressure reduction to 5 MPa over five days, and (2) maintaining a constant pressure of 5 MPa until the end of the simulation. Other parameters are detailed in Table 1 and Table 2.

Table 1 Parameters of the layers in hydrate reservoirs at the site SHSC2-6 (Data derived from Ye *et al.*, 2020, licensed under CC BY-NC-ND 4.0.).

Parameter	Layer				
	OB	GHBL	TPL	FGL	UB
Thickness/m	30	45.6	24.6	19	30
Porosity	0.373	0.373	0.346	0.347	0.347
Permeability/mD	1	2.38	6.63	6.8	1
Liquid saturation	1	0.69	0.751	0.927	1
Hydrate saturation	0	0.31	0.117	0.073	0
Gas saturation	0	0	0.132	0	0

Table 2 Parameters and models used in the simulations (Van Genuchten, 1980; Moridis *et al.*, 2005, 2007; Li *et al.*, 2017).

Parameter	Expression	value
Relative permeability model	$k_{\mathrm{relL}} = \left(\frac{S_{\mathrm{L}} - S_{\mathrm{Lr}}}{1 - S_{\mathrm{Lr}}}\right)^{n_{\mathrm{L}}}$ $k_{\mathrm{relG}} = \left(\frac{S_{\mathrm{G}} - S_{\mathrm{Gr}}}{1 - S_{\mathrm{Gr}}}\right)^{n_{\mathrm{G}}}$	$S_{\mathrm{Lr}} = 0.25$; $S_{\mathrm{Gr}} = 0.05$; $n_{\mathrm{L}} = 3.5$; $n_{\mathrm{G}} = 3.7$
Capillary pressure model	$P_{\mathrm{cap}} = -P_0\left[\left(\frac{S_{\mathrm{L}} - S'_{\mathrm{Lr}}}{1 - S'_{\mathrm{Lr}}}\right)^{-1/\lambda} - 1\right]^{1-\lambda}$	$P_0 = 10^5$; $S'_{\mathrm{Lr}} = 0.19$; $\lambda = 0.45$
Intrinsic permeability	$k_{\mathrm{h}} = k_0(1 - S_{\mathrm{H}})^N$	$N = 3$
Heat conduction coefficient (W/m/K)	$k_{\mathrm{T}} = k_{\mathrm{Tdry}} + \left(\sqrt{S_{\mathrm{L}}} + \sqrt{S_{\mathrm{H}}}\right)\left(\sqrt{k_{\mathrm{Twet}}} + \sqrt{k_{\mathrm{Tdry}}}\right)$	$k_{\mathrm{Tdry}} = 1.0$; $k_{\mathrm{Twet}} = 3.1$

3. Result and discussion

3.1 Model validation

3.1.1 Validation of the analytical theory

To validate the aforementioned analytical solution, a numerical model for hydrate exploitation via depressurization has been established based on OGS-Hydrate, as shown in Fig. 3. The main parameters are as follows: hydrate layer thickness H = 7 m, burden thickness b = 3 m, hydrate-bearing sediment intrinsic permeability k_{hbs} = 2.38 mD, burden intrinsic permeability $k^{'}$ = 1.0 mD, phase equilibrium conditions are 11.94 MPa, 286.465 K, the horizontal well is located in the middle of the reservoir with radius r_w = 0.12 m. The top and bottom boundaries of the model are prescribed as constant temperature and pressure. When the simulation reached a steady state, x^* is 11.67 m, closely matching the analytical prediction of 12.26 m, with a relative error (RE) of 4.8%, thereby indicating the accuracy of the solution. To further evaluate the applicability of the analytical solution under varying reservoir conditions, the impacts of b, k_{hbs}, P_w and H are investigated (Table 3).

Table 3 Sensitivity of the analytical solution to reservoir parameters.

Case	b (m)	k_{hbs} (mD)	P_w (MPa)	H (m)
Run1	3	2.38	5	7
Run2	30			
Run3	150			
Run4	300			
Run5	3	0.48		
Run6		11.9		
Run7		59.5		
Run8		2.38	1	
Run9			3	
Run10			7	
Run11			5	14
Run12				35
Run13				70

As shown in Fig. 4(a), the analytical solution predicts that the x^* expands with

318 increasing b. For burden thicknesses of 3 m, 30 m, 150 m and 300 m, the analytical
319 model predicts x^* of 11.42 m, 40.67 m, 90.79 m and 128.35 m, respectively. The
320 corresponding OGS-Hydrate simulation results are 11.67 m, 36.40 m, 87.0 m, and
321 128.40 m. The RE between the two remains within ±10%. In Fig. 4(b), the analytical
322 solution predicts that the x^* increases with k_{hbs}. When k_{hbs} is set to 0.476 mD, 11.9 mD,
323 and 59.5 mD, the predicted x^* from the analytical solution are 5.86 m, 28.79 m, and
324 64.24 m, respectively. The OGS-Hydrate simulation yields 5.95 m, 28.37 m, and 69.70
325 m, with the RE within ±10%. Fig. 4(c) illustrates that the analytically predicted x^* decreases
326 with the increasing P_w. When P_w is set to 1 MPa, 3 MPa, 5 MPa, and 7 MPa, the predicted x^*
327 from the analytical solution are approximately 15.18 m, 13.85 m, 12.26 m, and 10.27 m,
328 respectively. The corresponding OGS-Hydrate simulation yields 15.47 m, 13.59 m, 12.15 m,
329 and 10.14m. The RE between the two remains within ±10%. Similarly, Fig. 4(d) demonstrates
330 that x^* expands with increasing H. Across the evaluated range of H (from 7 m to 70 m), the
331 analytical predictions and numerical simulation results exhibit high consistency, with the RE
332 strictly bounded within ±10%. While the relative error (RE < 10%) demonstrates good overall
333 agreement, minor discrepancies inherently arise from the physical simplifications of the
334 analytical model. Specifically, unlike the numerical model, the analytical solution assumes a
335 constant absolute permeability (ignoring saturation-dependent variations), a sharp Stefan-type
336 dissociation interface (rather than a finite kinetic transition zone), and 1D linear flow
337 (neglecting near-well radial flow convergence).

338 3.1.2 Validation of the model under various gradients and well configurations

339 To validate Eq. (9), several simulation cases have been conducted, with detailed
340 parameters listed in Table 4. A schematic diagram of the simulation model is shown in
341 Fig. 5. In the table, the subscript B indicates cases accounting for variations in burden
342 intrinsic permeabilities. Among them, case Run_{B-2} features different intrinsic
343 permeabilities for OB and UB. In contrast, cases Run_{B-1} and Run_{B-3} assume identical
344 permeabilities for both layers, corresponding to the OB and UB permeabilities in Run_{B-2}, respectively. The geothermal and pressure (T-P) gradients influence P_e and P_{far} in the

analytical solution. In this study, the far-field temperature and pressure at the elevation of horizontal well are adopted as reference conditions. To account for the coupled effect of temperature and pressure on the production, the numerical model introduces both T-P gradients to verify the applicability of the analytical prediction under the stratified weighted average method. In addition, under constant T-P gradients, an increase in the burden thickness amplifies differences in temperature and pressure between the upper and lower boundaries. This also extends the mass and heat transfer paths to the horizontal well, which in turn affects the production effectiveness. To investigate this effect, cases with varying burden thicknesses are designed (Run_{G-1}, Run_{G-2}, Run_{G-3}). Finally, the Run_W series examines the effect of horizontal well configuration deviating from the reservoir center on the prediction accuracy; these models simultaneously consider the permeability differences between the OB and UB as well as the influence of T-P gradients.

Table 4 Parameters of the simulation models considering gradient and burden type.

Case	d (m)	k' (mD)	b (m)	k_{hbs} (mD)	H (m)
Run_{B-1}	3.5	1	3	2.38	7
Run_{B-2}		6.8			
Run_{B-3}		1			
Run_{G-1}		6.8	30		
Run_{G-2}		1	60		
Run_{G-3}			150		
Run_{W-1}	1.75	1	3		
Run_{W-2}	3.5				
Run_{W-3}	5.25				

Fig. 6 compares the x^* obtained from analytical solution prediction modified by the stratified weighted average method with that from numerical simulation. According to Eq. (9), the modified analytical solution (MAS) predicts x^* = 8.07 m in cases Run_{B-1} and Run_{B-3}, while the corresponding numerical simulation value in Run_{B-2} is 8.01 m. The RE between them is 0.07%, indicating strong agreement. The simulated x^* values in cases Run_{G-1}, Run_{G-2}, and Run_{G-3} are 37.55 m, 54.16 m, and 89.61 m, respectively,

with RE of 7.74%, 6.14%, and 0.01% compared to analytical predictions, showing good agreement. In the Run_W series, as horizontal well depth increases (from 1.75 m to 5.25 m), the simulated x^* are 7.76 m, 8.13 m, and 6.53 m, with REs of 3.35%, 9.83%, and 3.45%, respectively. Overall, the analytical predictions and simulation results are in good agreement across all cases. In summary, MAS for the x^* in hydrate exploitation via horizontal well depressurization, extended by the stratified weighted average method, can accurately capture the reservoir behavior under realistic conditions, including T-P gradients and horizontal well deviation from the reservoir center. This provides a valuable theoretical foundation for guiding productivity enhancement in field depressurization operations. It should be noted that the analytical solution yields satisfactory approximations for moderately to strongly anisotropic permeability (see Fig. C-3 in Appendix C). However, for fractured reservoirs, it is best applied to systems conceptualized as equivalent continuous media, serving only as an approximation for distinct dual-porosity systems. Additionally, while currently limited to single-well scenarios, extending the framework to address multi-well interference using superposition principles presents a viable avenue for future work.

3.1.3 Validation of high-efficiency production duration

Fig. 7(a) compares the time required for R_{out} to reach 60%, 70%, 80%, and 90% under different intrinsic permeability. The results show that as R_{out} increases, the time needed for a higher R_{out} increases significantly. Taking the case k_{hbs} = 2.38 mD as an example, reaching R_{out} = 60% requires 441 days, and each subsequent 10% increase in R_{out} demands 275, 521, and 2003 days, respectively. Notably, the time required to raise R_{out} from 80% to 90% is 3.84 times longer than the time needed for the 70% to 80% interval. In cases with k_{hbs} = 0.476 mD, 11.9 mD, and 59.5 mD, these multipliers are 3.48, 2.84, and 2.08, respectively, demonstrating a significant decline in exploitation efficiency during the late production stage. Fig. 7(b) shows the relative change rate (RC) of the time required for every 10% increase in recovery factor under four different k_{hbs}. When R_{out} reaches approximately 60%, an inflection point appears in the RC, which

then continuously rises, suggesting that the incremental time cost for achieving each additional 10% recovery increases substantially. The inflection point occurs at R_{out} of approximately 70% for k_{hbs} = 0.476 mD, 59.5 mD, and 11.9 mD. According to the technical guidelines for China's offshore oilfield development (Li *et al.*, 2019), production effectiveness is classified as Class I when the ratio of produced resources to original reserves is lower than 70%. Therefore, to ensure both a high recovery factor and adequate utilization of the reservoir's natural gas reserve, the time required to reach R_{out} = 70% is defined as the high-efficiency production duration. Correspondingly, combined with Eq. (8), 70% of the x^* is defined as the high-efficiency production zone $x^*_{0.7}$, and the associated natural gas reserve is the high-efficiency recoverable resource. These indicators can provide a theoretical basis for quantitative analysis for the optimization of depressurization schemes. Sensitivity analyses (see Fig. C-2 in Appendix C) indicate that this 70% threshold acts as a general theoretical indicator reflecting the reservoir's dominant heat and mass transfer capacities, as production efficiency is minimally sensitive to intrinsic hydrate dissociation kinetics.

3.2 Effects of reservoir types and well configurations

3.2.1 Characteristics of hydrate dissociation and gas-liquid migration

Fig. 8 presents the spatial distribution of hydrate saturation at 1 year and 10 years of depressurization-driven production for Class I, Class II and Class III reservoirs with different well configurations. The yellow curve represents the hydrate dissociation boundary. As described in Fig. 8(a), the hydrate dissociation boundary moves downward rapidly due to the influence of the T-P gradients in the Class I reservoir. After 1 year of production, the hydrate dissociation boundaries in cases I_{upper}, I_{middle} and I_{lower} exhibit similar morphologies. In case I_{upper}, the dissociation boundary has not yet reached the upper GHBL boundary, whereas in case I_{lower}, it has extended to the bottom of the GHBL. After 10 years, the upper part of the dissociation boundary in case I_{upper} reaches the upper GHBL boundary, and its lower part connects to the lower GHBL

boundary. In case I_{middle}, the upper part of the dissociation boundary is located approximately 15 m below the upper GHBL boundary, while the lower part connects to the lower GHBL boundary and extends laterally along the interlayer to the model's horizontal boundary. In case I_{lower}, the upper part of the dissociation boundary remains about 31 m below the upper GHBL boundary and similarly propagates along the interlayer to the left model boundary.

As depicted in Fig. 8(b), after 1 year of production, the hydrate dissociation boundary propagation in the Class II reservoir cases resembles that in Class I, although it lags slightly behind. After 10 years of exploitation, the difference in the dissociation boundary development between Class I and Class II reservoirs becomes more pronounced. The horizontal extent of the dissociation boundary in case II_{upper} lags about 20 m behind that in case I_{upper}, while that in case II_{middle} lags approximately 30 m behind that in case I_{middle}. In contrast, the hydrate dissociation zone in case II_{lower} is larger than that in case I_{lower}. As illustrated in Fig. 8(c), the hydrate distribution and the morphology of the hydrate dissociation boundary in all Class III cases exhibit no significant difference compared with the corresponding Class I and Class II cases. However, owing to the low permeability of the UB, heat transfer is restricted, causing a slower downward propagation of the dissociation boundary relative to that in Class II during the same period.

To quantitatively evaluate the hydrate dissociation efficiency and the total amount of dissociation, this study employs the hydrate dissociation degree (Ye *et al*., 2025), and further defines the hydrate dissociation degree within the dissociated zone ($D_{\mathrm{H\_D}}$) and the hydrate dissociation degree in the GHBL ($D_{\mathrm{H\_GHBL}}$), which are expressed as follows, respectively:

$$D_{\mathrm{H\_D}} = 1 - \frac{S_{\mathrm{Ht\_D}}}{S_{\mathrm{Ho\_D}}} \tag{11a}$$

$$D_{\mathrm{H\_GHBL}} = 1 - \frac{S_{\mathrm{Ht\_GHBL}}}{S_{\mathrm{Ho\_GHBL}}} \tag{11b}$$

where D is the hydrate dissociation degree, S_{H} represents hydrate saturation, 0 stands

for initial state, *t* refers to final state, subscript D denotes the hydrate dissociation zone, GHBL stands for the GHBL domain. D_{H_GHBL} reflects the proportion of the total amount of hydrate dissociation in the hydrate layer. D_{H_D} reflects the hydrate dissociation efficiency within the dissociated zone, as well as the gap between the dissociation boundary and x^*; when production reaches a steady state, the dissociation boundary no longer expands, and D_{H_D} approaches 1.

Fig. 9 displays the evolution of D_{H_D} and D_{H_GHBL} over time, where different line colors represent different reservoir types. As shown in Fig. 9(a), the D_{H_GHBL} for all cases gradually increases over time. In the early stage, D_{H_GHBL} in case III_{lower} is higher than that in I_{lower} and comparable to II_{lower}. However, as production proceeds, its growth rate slows down; after 4.5 years of production, it is lower than that in case II_{lower}, and after 8 years, it is slightly below I_{lower}. After 10 years, D_{H_GHBL} for cases III_{lower}, II_{lower}, and I_{lower} are 0.12, 0.13, and 0.12, respectively. Regarding the well configuration, D_{H_GHBL} exhibits the largest value in case I_{lower} and the lowest in I_{upper}. Furthermore, D_{H_GHBL} in Class II and Class III follows the same trend. This is because a deeper horizontal well depth corresponds to a higher ambient temperature and a shorter heat transfer distance, thus enhancing hydrate dissociation. After 10 years, the D_{H_GHBL} values for horizontal well in the upper and middle parts are similar among the three reservoir types, with values of 0.09 and 0.11 for cases I_{upper} and I_{middle}, respectively. This indicates that the reservoir type exerts little influence on the hydrate dissociation when the horizontal well is positioned in the upper and middle parts.

Regarding D_{H_D}, as depicted in Fig. 9(b), its development trend is similar to D_{H_GHBL}, exhibiting continuous growth over time. In the early stage, when the horizontal well is placed in the upper and middle part of GHBL, D_{H_D} initially decreases and then rises after reaching a local peak. The timing of this inflection point is delayed as the horizontal well depth increases. In contrast, when the horizontal well is placed in the lower GHBL, D_{H_D} shows no obvious decrease. For case I_{upper}, the inflection point appears at about 1 year of production, coinciding with the time when the hydrate

dissociation boundary reaches the lower boundary of the hydrate layer in Fig. 8(a). It indicates that the higher ambient temperature at depth enhances the hydrate dissociation efficiency. When the horizontal well is placed in the middle of the GHBL, D_{H_D} in case III_{middle} is the highest. This is because the low permeability of the burden limits heat transfer, resulting in a smaller dissociation range; however, it also suppresses seawater intrusion and maintains a more efficient depressurization. As production proceeds, the D_{H_D} in case I_{middle} gradually becomes lower than that in II_{middle}, owing to the inhibition of mass and heat transfer by free gas and the enhanced seawater intrusion facilitated by the underlying high-permeability soil layer, decreasing hydrate dissociation efficiency. After 10 years, the D_{H_D} is highest in case I_{lower} and lowest in I_{up}, a trend which is also observed in Class II and Class III. In terms of reservoir type, the D_{H_D} evolution curves in cases I_{upper}, II_{upper}, and III_{upper} are nearly identical. After 10 years, D_{H_D} in case I_{upper} is 0.304, closely matching the other two, indicating that the reservoir type has no significant effect on D_{H_D} for the upper well placement. For the middle and lower well placements, D_{H_D} in cases III_{middle} and III_{lower} are the highest, respectively reaching 0.41 and 0.52, indicating that the low-permeability underlying layer helps to improve the degree of hydrate dissociation within the dissociated zone. In summary, D_{H_GHBL} ranges between 0.09 and 0.13 across all cases, while D_{H_D} ranges between 0.30 and 0.52. These reveal that although the dissociation domain expands relatively rapidly, the available heat within the zone is insufficient, resulting in low hydrate dissociation efficiency, and a limited overall hydrate dissociation amount.

As illustrated in Fig. 10(a), after 1 year of production, the gas saturation distribution around the production well in cases I_{upper}, I_{middle}, and I_{lower} are detailed. Among them, the FGL gas saturation in case I_{lower} has already invaded the GHBL and connected with the gas produced from hydrate dissociation around the horizontal well. After 10 years, the FGL gas saturation in case I_{upper} has only partially invaded the GHBL and remains unconnected to the horizontal well, with no significant liquid invasion observed from the underlying layer. Conversely, in cases I_{middle} and I_{lower}, the FGL gas

saturation has extensively invaded the GHBL, accompanied by liquid invasion. In Fig. 10(b) and Fig. 10(c), under the same well configuration scenario, the gas saturation distribution in Class II and Class III reservoirs closely resemble those of Class I. For cases where the horizontal well is placed in the upper or middle GHBL, the liquid saturation from the underlying soil layers has not invaded the vicinity of the horizontal well after 10 years. As for cases II_{lower} and III_{lower}, after 10 years, the liquid phase has invaded the zone surrounding the horizontal well, and gas saturation generated from hydrate dissociation is visible along the lower boundary of the hydrate layer. Compared with case II_{lower}, the extent of gas saturation expansion in III_{lower} is smaller, which corresponds to the aforementioned hydrate dissociation boundary and dissociation degree.

3.2.2 Characteristics of gas and water production

Fig. 11 describes the gas and water production characteristics for different reservoir types and well configurations. As shown in Fig. 11(a), the cumulative gas production in the Class I reservoir is higher than that in Class II and Class III, due to the contribution from the free gas in the FGL. After 10 years of production, the cumulative gas production in cases I_{middle} and I_{lower} reaches 9.62×10^6 m^3 and 1.22×10^7 m^3, respectively. However, when the horizontal well is placed in the upper part of the GHBL, the cumulative gas production among the three reservoir types is comparable. This means that the reservoir type has no significant effect on gas production, with the cumulative gas production in case I_{upper} being 6.67×10^6 m^3. Regarding the well configuration effect, in Class I and Class III, the lower the well configuration, the higher the cumulative gas production. However, in Class II, case II_{lower} yields a cumulative gas production of 8.48×10^6 m^3 after 10 years, which is lower than that in case II_{middle} (8.75×10^6 m^3), on account of the high-permeability FWL exacerbating seawater intrusion.

Fig. 11(b) presents that the influence of reservoir type on gas production rate becomes more pronounced when the horizontal well configuration is placed in both the

middle and the lower part of the GHBL. The gas production rates for different well configurations gradually diverge over time, with the onset of these differences occurring earlier as the horizontal well depth increases. After 1.5 years of production, the gas production rate in case I_{lower} increases due to the free gas invasion from the FGL, exceeding those from II_{lower} and III_{lower}, and reaching a second peak of 4.00×10^3 m^3/day at 2.9 years. The gas production rate in case I_{middle} continuously increases after 4 years, surpassing those in II_{middle} and III_{middle}, and reaching 2.67×10^3 m^3/day at 10 years. During the stable depressurization stage, the gas production rates for cases well placed in the upper GHBL in all reservoir types show a continuous decline, with no significant difference in magnitude. This is attributed to the fact that the longer seepage path weakens the influence of the reservoir type on the gas production rate. Regarding the influence of well configuration, the gas production rate during the early stage of production in Class I is ranked as follows: $I_{lower} > I_{middle} > I_{upper}$, a trend which is also observed in Class II and Class III reservoirs. However, as production proceeds, the gas production rates in cases I_{lower}, II_{lower}, and III_{lower} fall below those in I_{middle}, II_{middle}, and III_{middle} after 3.4 years, 6.5 years, and 8.4 years, respectively. Notably, after 9 years of production, the gas production rate in case II_{lower} is even lower than that in II_{upper}.

Fig. 11(c) shows that the cumulative water production is highest when the horizontal well is placed in the lower part of the GHBL, and lowest in the middle part. This is because a horizontal well placed in the middle of the GHBL can reduce seawater intrusion from adjacent layers. The high-permeability FWL in Class II enhances seawater intrusion, resulting in a cumulative water production of 1.52×10^6 m^3 in case II_{lower} after 10 years. In contrast, although the FGL in Class I has the same intrinsic permeability as the FWL, the cumulative water production in case I_{lower} (1.31×10^6 m^3) is lower than that in case II_{lower} and close to III_{lower}. Similarly, for the middle well configuration, the cumulative water production in case I_{middle} is also slightly lower than that in III_{middle}. This is mainly because gas phase flow in the FGL during production hinders the liquid invasion, thereby reducing water production.

Fig. 11(d) illustrates that the water production rate in case I_{lower} is lower than that in III_{lower} after 1 year of production, but surpasses it after 4 years, leading to comparable cumulative water production after 10 years. This is attributed to the replenishment of free gas from the FGL in the initial stage, which elevates gas saturation and hinders liquid flow, while the subsequent gas saturation reduction intensifies liquid invasion. For cases well placed in the upper GHBL, the water production rate exhibits a similar evolution among all reservoir types, among them, with case I_{upper} reaching 3.27×10^3 m^3/day after 10 years. In contrast, when the horizontal well is placed in the lower part of the GHBL, the water production rate is significantly higher than that in the other two well configurations, reaching 5.05×10^3 m^3/day in case II_{lower} after 10 years.

As depicted in Fig. 11(e), the initial gas water ratio (GWR) increases with well depth across all reservoir types, reaching a peak in the early stage, and then gradually decreasing over time. Among them, when the horizontal well is placed in the lower part of the GHBL, the GWR is initially higher. However, as production proceeds, the gas production rate decreases while liquid invasion enhances and water production increases, leading the GWR to decline more rapidly than that in other well configurations. Specifically, around 1 year of production, the GWRs in cases II_{lower} and III_{lower} successively fall below that in II_{middle} and III_{middle}, respectively. At 4.5 years, the GWR in case II_{lower} becomes lower than that in II_{upper}, and by 10 years, the GWR in III_{lower} also falls below that in III_{upper}. Similarly, although case I_{lower} has a higher GWR in the early stage due to the contribution of free gas, its GWR also decreases rapidly as production proceeds. For example, the GWR in case I_{lower} is lower than that in I_{middle} after 6 years, and falls below that in II_{middle} and III_{middle} after 10 years.

3.2.3 Evaluation of Exploitation Efficiency

Fig. 12 shows R_{out} and the average value of the hydrate dissociation boundary (x_{10yr}) after 10 years of production simulated with OGS-Hydrate, and the analytically predicted high-efficiency production zone ($x^*_{0.7}$) for each case. The blue dotted line represents x^* in each case, which gradually increases as the horizontal well depth

increases. For Class I and Class II reservoirs, x^* rises from 56.21 m to 112.42 m as the well shifts from the upper GHBL to the lower. For the Class III reservoir, x^* values in III_{upper}, III_{middle}, and III_{lower} are 68.91 m, 89.97 m, and 125.81 m, respectively. These values are slightly higher than those in cases with the same well configuration for Class I and Class II reservoirs, due to the sealing burden. The red dotted line represents x_{10yr}. Compared with the analytical prediction of $x^*_{0.7}$, there is a large gap for x_{10yr} in all cases after 10 years, indicating a slower development of the hydrate dissociation boundary. Moreover, x_{10yr} gradually increases with well depth, with values of 33.22 m, 46.64 m, and 48.13 m in cases I_{upper}, I_{middle}, and I_{lower} , respectively, reaching 59.1%, 60.7%, and 42.8% of their corresponding $x^*_{0.7}$. The x_{10yr} values in II_{upper}, II_{middle}, and II_{lower} are 24.67 m, 38.19 m, and 48.63 m, respectively, reaching 43.9%, 49.7%, and 43.3% of their corresponding $x^*_{0.7}$. The x_{10yr} values for III_{upper}, III_{middle}, and III_{lower} are 27.55 m, 28.04 m, and 35.05 m, respectively, reaching 34.0%, 27.4%, and 25.3% of their corresponding $x^*_{0.7}$.

R_{out} can be used to quantify the degree of reservoir exploitation, as its value synthetically reflects the mass and heat transfer processes within the reservoir. The bar chart shows that R_{out} in all cases is below 0.15, indicating that the gas production potential remains underutilized after 10 years of production. For the Class I reservoir, the R_{out} values are highest in case I_{middle}, intermediate in I_{upper} and lowest in I_{lower}. In the Class II reservoir, case II_{upper} exhibits the highest R_{out}, while case II_{lower} shows the lowest. This occurs because the FGL free gas in Class I is more readily produced than hydrates in Class II, resulting in a higher R_{out} in case I_{lower} compared to case II_{lower}. Although the analytically predicted $x^*_{0.7}$ in Class III is higher, after 10 years of production, their corresponding R_{out} values (0.08, 0.08, and 0.06) are slightly lower than those in Class I and Class II reservoirs. This is because the low permeability of the reservoir limits the mass and heat transfer, preventing the full release of gas production potential within the 10-year production period.

3.3 Hydrate productivity prediction in the Shenhu area of the South China Sea

3.3.1 Characteristics of gas and water production

Fig. 13 presents the gas and water production characteristics of the second hydrate production test in the South China Sea. Cases Mid_{TPL} and Mid_{GHBL} denote the two cases where the horizontal well is placed in the middle of the TPL and the GHBL, respectively. As shown in Fig. 13(a), the cumulative gas production in case Mid_{TPL} reaches $8.85 \times 10^5\ m^3$ after 30 days. The long-term production is also comparable to previous one-year simulations (Xiao *et al.*, 2022; Yin *et al.*, 2022). Compared with the field-measured 30-day gas production of $8.61 \times 10^5\ m^3$, the RE is 2.73%, indicating good agreement and validating the model's accuracy. After 10 years of simulated production, the cumulative gas production in the Mid_{GHBL} and Mid_{TPL} cases reaches $1.21 \times 10^7\ m^3$ and $2.20 \times 10^7\ m^3$, respectively. The gas production evolution of the two cases differs markedly. In case Mid_{GHBL}, the gas production rate remains stable without noticeable fluctuations, and the cumulative gas production curve exhibits an almost linear growth trend. In case Mid_{TPL}, the gas production rate gradually declines after reaching an initial peak of $4.35 \times 10^4\ m^3$/day, and after 10 years, it approaches that in case Mid_{GHBL}.

Fig. 13(b) shows the cumulative water production and water production rate curves in cases Mid_{TPL} and Mid_{GHBL}. In case Mid_{GHBL}, as production proceeds, hydrate dissociation in the GHBL increases the permeability of the dissociated zone and generates water, jointly leading to a slow rise in the water production rate. In contrast, the water production rate in case Mid_{TPL} decreases during the early stage of production but begins to rise after 1 year. After 10 years of production, the cumulative water production in cases Mid_{GHBL} and Mid_{TPL} is $1.09 \times 10^6\ m^3$ and $2.18 \times 10^6\ m^3$, respectively.

3.3.2 Reservoir permeability enhancement and production prediction

Low reservoir permeability is one of the key factors limiting the efficiency of mass and heat transfer during hydrate exploitation, and enhancing reservoir permeability is regarded as an effective way to improve productivity. As discussed from the previous

section, case Mid_{TPL} exhibits higher gas production. Therefore, taking the intrinsic permeability of the TPL hydrate-free sediment (k_{sed_TPL} = 9.6 mD) as a reference, x^* in case Mid_{TPL} and the corresponding recoverable natural gas volume per unit well length under different multiples of k_{sed_TPL} are calculated using Eq. (8) and Eq. (9). While assuming a spatially uniform permeability enhancement is an idealization that may overestimate actual field performance compared to explicit fracture modeling, this parametric approach is adopted to establish a theoretical upper limit for recoverability. This simplified approach intentionally isolates the impact of permeability magnitude, avoiding the profound uncertainties and complex thermal-hydro-mechanical-chemical couplings associated with discrete fracture networks (DFN) that currently lack sufficient field calibration data (Zhang *et al*., 2024). On this basis, the minimum horizontal well length (L_{min_10yr}) required to achieve the 10-year commercial production target (2.0×10^5 m^3/day) is further determined according to the natural gas reserves within the high-efficiency production range.

Fig. 14 depicts the analytically predicted L_{min_10yr}, and the simulation L_{min_10yr} without and with sufficient heat (zero dissociation enthalpy), to respectively represent theoretical and actual conditions. Among them, the blue curve represents the analytically predicted L_{min_10yr}. As the intrinsic permeability increases, L_{min_10yr} gradually decreases. For example, L_{min_10yr} is 709.6 m under the $5k_{sed\_TPL}$ condition, 409.9 m under $15k_{sed\_TPL}$ (144 mD), and 317.6 m under $25k_{sed\_TPL}$ (240 mD). The depressurization case (Mid_{TPL_ST}) that neglects the endothermic heat of hydrate dissociation represents the situation where only mass transfer, as assumed by the analytical theory, is considered. As shown by the red dots in Fig. 14, the required well lengths for commercial production in case Mid_{TPL_ST} at $5k_{sed\_TPL}$, $15k_{sed\_TPL}$, and $25k_{sed\_TPL}$ are 835.10 m, 407.69 m, and 300.32 m, respectively, showing good agreement with the theoretical predictions. As depicted by the red dotted line, when considering the actual heat transfer, L_{min_10yr} becomes much larger than the analytical prediction. The simulated L_{min_10yr} in case Mid_{TPL} is 2904.90 m at $5k_{sed\_TPL}$, 1474.3 m

673 at $15k_{sed\_TPL}$, and 1147.50 m at $25k_{sed\_TPL}$. As the reservoir intrinsic permeability
674 increases, mass and heat transfer are accelerated, causing L_{min_10yr} in Mid_{TPL} to
675 approach the analytical expectation. However, even at $25k_{sed\_TPL}$, the required well
676 length still reaches 1147.50 m.

677 Fig. 15(a) shows the analytically predicted $x^*_{0.7}$, x_{10yr}, and the simulated 10-year
678 R_{out} in cases Mid_{GHBL} and Mid_{TPL} with different permeabilities. The analytically
679 predicted $x^*_{0.7}$ in Mid_{GHBL} is larger than that in Mid_{TPL}, reaching 198.7 m and 135.9 m,
680 respectively. As the intrinsic permeability of case Mid_{TPL} increases from $5k_{sed\_TPL}$ to
681 $25k_{sed\_TPL}$, the predicted $x^*_{0.7}$ gradually rises to 333.1 m, 577.0 m, and 744.9 m,
682 respectively. After 10 years of simulation, x_{10yr} in Mid_{GHBL} is 36.8 m, accounting for
683 only 18.5% of the analytically predicted $x^*_{0.7}$, indicating a significant discrepancy
684 between the theoretical prediction and the simulated result. Furthermore, R_{out} is only
685 0.05. In case Mid_{TPL}, x_{10yr} is 68.8 m, corresponding to 50.6% of $x^*_{0.7}$, and R_{out} is 0.20.
686 Although the analytically predicted $x^*_{0.7}$ is larger, both x_{10yr} and R_{out} are lower than
687 those in Mid_{TPL}, as the low-permeability hydrate layer limits the mass and heat transfer,
688 leading to slower hydrate dissociation boundary development and gas migration. As the
689 intrinsic permeability of case Mid_{TPL} increases from $5k_{sed\_TPL}$ to $25k_{sed\_TPL}$, the pressure
690 propagation accelerates, the discrepancy between x_{10yr} and the prediction narrows,
691 reaching 70.5%, 85.8%, and 89.6% of the corresponding $x^*_{0.7}$, respectively. During this
692 process, R_{out} first increases and then decreases with increasing reservoir intrinsic
693 permeability. After 10 years of production, R_{out} ranges from 0.18 to 0.21. Even under
694 high permeability conditions, the gas production potential is not fully released within
695 the limited production period. However, in case Mid_{TPL_ST} at $5k_{sed\_TPL}$, the value of R_{out}
696 is 0.63, significantly higher than other cases. Further comparison of case Mid_{TPL_ST}
697 with different permeabilities shows that the R_{out} at $15k_{sed\_TPL}$ and $25k_{sed\_TPL}$ are 0.75
698 and 0.90, respectively. R_{out} increases significantly with intrinsic permeability, enabling
699 better utilization of gas production potential within a limited time.

700 Fig. 15(b) describes the cumulative gas production per unit horizontal well length

for different cases. The solid line denotes case Mid_{TPL} considering the actual heat transfer, and the dashed line corresponds to case Mid_{TPL_ST} with sufficient heat supply. As the reservoir intrinsic permeability increases, the cumulative gas production per unit horizontal well length gradually increases. When the intrinsic permeability of case Mid_{TPL} increases from k_{sed_TPL} to $25k_{sed\_TPL}$, the cumulative gas production increases from 7.84×10^4 m^3 to 6.36×10^5 m^3. Specifically, for permeability intervals of 5-15k_{sed_TPL} and 15-25k_{sed_TPL}, the cumulative gas production increases by 97.03% and 28.48%, respectively. In case Mid_{TPL_ST} at $5k_{sed\_TPL}$, initially produces less gas than Mid_{TPL} at $25k_{sed\_TPL}$ due to its lower permeability. However, as production proceeds, case Mid_{TPL_ST} at $5k_{sed\_TPL}$ surpasses Mid_{TPL} at $25k_{sed\_TPL}$ after 1 year due to sufficient heat supply, reaching a cumulative gas production of 8.74×10^5 m^3 after 10 years. In case Mid_{TPL_ST} at $15k_{sed\_TPL}$ and $25k_{sed\_TPL}$, the cumulative gas production reaches 1.79×10^6 m^3 and 2.43×10^6 m^3, respectively. For the intervals of 5-15k_{sed_TPL} and 15-25k_{sed_TPL}, the cumulative gas production increases by 104.84% and 35.75%, respectively.

To evaluate the production efficiency of NGHs, this study adopts the energy return on investment (EROI) analysis method following the work of Lior (2016), Kong *et al.* (2018) and Wei *et al.* (2022). The detailed calculation procedure is provided in Appendix B. The analysis results are shown in Fig. 16, which presents the E_{in} and $EROI_{ues}$ corresponding to the required well lengths for commercial production in case Mid_{TPL} under different permeability conditions, where E_{out} remains 2.61×10^7 GJ in all cases. The $EROI_{ues}$ exhibits a trend of first increasing and then decreasing as permeability increases, reaching a peak value of 1.08 at $15k_{sed\_TPL}$.

3.4 Discussion

3.4.1 Mass and heat transfer during different exploitation stages

The hydrate exploitation lifecycle can be conceptually divided into a pressure-controlled stage and a heat-controlled stage. In the early stage of depressurization, the

pressure drop acts as the primary driving force (Cheng *et al.*, 2024). Consequently, the low-permeability burden in Class III reservoirs initially promotes the development of the depressurization zone, temporarily enhancing dissociation. However, as production proceeds, the governing factor transitions from depressurization to heat supply (Song *et al.*, 2015; Kou *et al.*, 2019; Zhao *et al*., 2021; Yin *et al*., 2022). The low-permeability burden, which initially aided depressurization, subsequently becomes a hindrance by suppressing heat convection. This explains why the hydrate dissociation degree in Class III reservoirs gradually falls below that of Class I and Class II in the later stages. In Fig. 8, this transition from pressure-driven to heat-driven dissociation is further evidenced by the contrasting behaviors of Class I and Class II reservoirs. In Class I reservoirs, the presence of free gas in the FGL initially enhances pressure transmission along the interlayer, consistent with the findings reported by Moridis *et al.* (2007). However, gas migration in the FGL subsequently hinders liquid intrusion, and the free gas possesses a low specific heat capacity, leading to delayed development of the dissociation zone in the later stage. Conversely, when the horizontal well is positioned in the lower part of a Class II reservoir, seawater intrusion from the high-permeability free water layer (FWL) provides convective heat for hydrate dissociation, sustaining higher dissociation rates.

3.4.2 Gas and liquid invasion under different well placement modes

As illustrated by the spatial distribution of gas saturation (Fig. 10), the distinct invasion patterns of gas and liquid are fundamentally driven by their physical properties. Gas, characterized by lower viscosity and higher mobility, migrates rapidly, resulting in an invasion pattern that is less sensitive to well placement. In contrast, the liquid invasion pattern is significantly influenced by the well placement, making the vertical position of the horizontal well a critical determinant of water production behaviors. Optimizing the well vertical placement involves a trade-off between thermal stimulation and water management. Placing the horizontal well in the lower part of the GHBL effectively utilizes the geothermal heat supply from the underlying layer to

promote hydrate dissociation. However, as depicted in the production characteristics (Fig. 11), this configuration significantly exacerbates water production, leading to a rapid decline in GWR. Therefore, for long-term production, positioning the horizontal well in the middle of the GHBL appears more favorable for maintaining high production efficiency, as it balances heat utilization with the suppression of excessive water intrusion.

The significance of this middle placement is further demonstrated in the Shenhu area case study. As shown in Fig. 13, case Mid_{TPL} initially yields high gas production because it involves a higher proportion of free gas extraction. However, as the free gas is produced, the proportion of natural gas originating from hydrates increases, leading to greater production difficulty and a severe decline in the gas rate. Furthermore, gas accumulation in the TPL initially hinders liquid flow, but as production proceeds, liquid invasion and gas production reduce the gas saturation near the wellbore, thereby increasing the liquid relative permeability and water production rate. The higher permeability TPL and FGL enhance seawater intrusion and water production, whereas placing the well in the low-permeability GHBL effectively suppresses excessive water influx, leading to a larger amount of ultimate water production in Mid_{TPL} than in $Mid_{GHBL.}$

Beyond the physical mechanisms, the evaluation of exploitation efficiency highlights a critical challenge: the reservoir production potential remains largely underutilized. Although the dissociation domain expands relatively rapidly, the available heat within the zone is often insufficient, resulting in low hydrate dissociation efficiency and a limited overall recovery factor (R_{out}). Enhancing productivity in horizontal well depressurization requires not only expanding the single-well recoverable zone but also ensuring that the production potential is fully released within the production cycle. This necessitates optimizing the reservoir's mass and heat transfer processes through assisted production enhancement methods.

3.4.3 Energy efficiency of permeability enhancement

Simulation results indicate that when reservoir intrinsic permeability is enhanced, heat transfer becomes the dominant factor controlling production. Under sufficient heat supply, the production enhancement resulting from increased permeability becomes significantly more pronounced. Therefore, balancing heat supplementation and permeability enhancement in the design of stimulation strategies is essential to achieve greater production improvement. Studies have shown that the intrinsic permeability of offshore hydrate reservoirs after fracturing can reach 5.75 D. In practical engineering, while technologies such as hydraulic fracturing can locally improve reservoir permeability, developing and sustaining an effective fracture network within the horizontal well's recovery zone remains a formidable challenge (Cipolla *et al.*, 2008; Qi *et al*., 2025).

The trade-off between energy input and gas recovery dictates an optimal permeability enhancement range. As shown in Fig. 16, the emergence of an EROI peak is primarily related to variations in energy input (E_{in}). As reservoir permeability increases, the required well length for commercial production decreases, reducing drilling costs. However, since E_2 accounts for only a small fraction of E_{in}, its impact on the overall energy input is limited. On the other hand, higher reservoir permeability intensifies mass transfer, causing E_3, which accounts for the largest proportion, to vary significantly with water production and well length. Therefore, from the perspective of maximizing net energy return, it is recommended to control the reservoir permeability enhancement target below $15k_{\mathrm{sed\_TPL}}$.

4. Conclusion

This study verifies the effectiveness of the analytical solution for the maximum recoverable zone via hydrate horizontal well depressurization method (Terzariol *et al.* 2017) using the OGS-Hydrate numerical simulation results (Ye *et al.*, 2022), and further proposes a modified analytical solution (MAS) to broaden its application scope. Several

indicators are proposed to evaluate the production efficiency in horizontal well depressurization. In combination with MAS, these indicators are employed to assess the effects of different reservoir types and well configuration schemes on productivity and production potential. The required well length for commercial production is predicted under various permeability conditions for the hydrate reservoir in the Shenhu area of the South China Sea. Furthermore, the impacts of mass and heat transfer optimization methods on production potential and efficiency are systematically analyzed. The main conclusions are as follows:

(1) Based on the analytical solution to the maximum recoverable zone, a modified analytical solution (MAS) is proposed by extending the application scope with stratified weighted average method. It enables the prediction of the maximum recoverable zone under various conditions, including different burden permeabilities, temperature-pressure (T-P) gradients, and horizontal well configurations. The RE with simulation results is within 10%, showing good agreement. Furthermore, the MAS is applied to predict the recoverable zone with permeability enhancement and the commercial horizontal well length for the hydrate reservoir in the Shenhu area of South China Sea.

(2) A recovery factor (R_{out}) associated with the maximum recoverable zone (x^*) is proposed to evaluate the NGH production efficiency during horizontal well depressurization. Under different GHBL permeabilities, the time required to increase R_{out} from 80% to 90% is approximately 2.08-3.84 times that required for an increase from 70% to 80%. The transition stage in the relative change rate of R_{out} occurs at around 70%. Accordingly, the occupation of 70% natural gas reserve within x^* is defined as the high-efficiency production zone.

(3) Reservoir type leads to different gas-liquid invasion patterns, which significantly affects production behavior. In Class I, gas invasion hinders liquid-phase heat transfer, thereby restricting hydrate dissociation. Class II shows the lowest gas production and the highest water production due to the high-permeability FWL enhancing liquid invasion. In contrast, Class III surpasses Class II in gas recovery via

efficient pressure-driven gas migration, compensating for the limited liquid and heat recharge. The gas-liquid invasion process is also affected by the horizontal well configuration. Placing the well in the middle GHBL is more suitable for long-term production with the highest gas production rate and gas water ratio after 10 years. Moreover, the R_{out} in all cases is below 0.15, indicating that low-permeability reservoirs face challenges in fully utilizing their depressurization production potential within a reasonable period.

(4) Under different permeability conditions, limited heat transfer dominates the production process. The well length required for commercial production obtained from numerical simulation is approximately 3.61-4.09 times that predicted by the MAS considering NGH within $x^*_{0.7}$. Moreover, the R_{out} remains low, ranging from 0.18 to 0.21 within 10 years, where it can reach 0.63-0.90 under sufficient heat supply conditions. These indicate that achieving commercial exploitation should involve a combined strategy of permeability enhancement and thermal stimulation. Based on the EROI analysis, the practical permeability enhancement target is recommended to be below $15k_{sed\_TPL}$.

CRediT authorship contribution statement

Bin Zhu: Supervision, Conceptualization, Methodology, Project administration, Writing - review and editing.

Ronghan Guo: Writing - original draft, Conceptualization, Methodology, Validation, Writing - review and editing.

Zhigang Ye: Supervision, Conceptualization, Methodology, Software, Validation, Writing - review and editing.

Shao Haibing: Supervision, Conceptualization, Methodology, Writing - review and editing.

Lujun Wang: Supervision, Conceptualization, Methodology, Project administration, Writing - review and editing.

Acknowledgement

The authors acknowledge the funds from the National Natural Science Foundation of China (Nos. 52588202, 52127815). Additionally, the authors acknowledge the use of ChatGPT to improve the language, grammar, and readability of the manuscript. The authors reviewed and edited the output as needed and take full responsibility for the content of the publication.

Appendix A

For the completeness of the paper, we briefly present the system of equations that describe the mathematical model of the maximum recoverable zone under horizontal well depressurization. The model is established based on a conceptual physical scenario with the following assumptions: (1) horizontal well length $L \gg H$; (2) the horizontal well is drilled parallel to the formation along the reservoir center; (3) darcy seepage is considered. Mass conservation across a slice of the reservoir of thickness dx with leak-in from upper and lower burdens results in:

$$\frac{\partial^2 \bar{\bar{P}}}{\partial x^2} - \frac{\bar{\bar{P}}}{\lambda_{sed}^2} = 0 \tag{A-1}$$

where $\bar{\bar{P}} = P_{\mathrm{x}} - P_{\mathrm{far}}$.

$$P_{\mathrm{x}} = P_{\mathrm{far}} + Ae^{\left(\frac{x}{\lambda}\right)} + Be^{\left(-\frac{x}{\lambda}\right)} \tag{A-2}$$

The seepage equations within the hydrate-free sediment zone and the hydrate-bearing sediment zone are respectively:

$$q_{\mathrm{sed}} = \frac{2LH}{\lambda_{\mathrm{sed}}} \frac{k_{\mathrm{sed}}}{\gamma_{\mathrm{w}}} \left[A_{\mathrm{sed}} e^{\left(\frac{x}{\lambda_{\mathrm{sed}}}\right)} - B_{\mathrm{sed}} e^{\left(-\frac{x}{\lambda_{\mathrm{sed}}}\right)} \right] \tag{A-3}$$

$$q_{\mathrm{hbs}} = \frac{2LH}{\lambda_{\mathrm{hbs}}} \frac{k_{\mathrm{hbs}}}{\gamma_{\mathrm{w}}} (P_{\mathrm{far}} - P^*) e^{\left(\frac{x^* - x}{\lambda_{\mathrm{sed}}}\right)} \tag{A-4}$$

The water flow rate in the inner and outer zones must be equal $q_{\mathrm{sed}} = q_{\mathrm{hbs}}$ when $x = x^*$. Then, Equations (A-3) and (A-4) predict:

$$\frac{\left[\mathrm{A_{sed}}\, \mathrm{e}^{\frac{x^*}{\lambda_{\mathrm{sed}}}} - \mathrm{B_{sed}}\, \mathrm{e}^{\frac{x^*}{\lambda_{\mathrm{sed}}}} \right]}{(P_{\mathrm{far}} - P^*)} = \frac{\sqrt{k_{hbs}}}{\sqrt{k_{sed}}} \tag{A-5}$$

Considering boundary conditions: (a) x→∞, $u_x = u_{far}$; (b) when $x \rightarrow r_w$, $u_x = u_w$; A_{sed} and B_{sed} can be obtained, and the final solution is shown in Equation (8).

Appendix B

The EROI was calculated with reference to the methods of Lior (2016), Kong *et al.* (2018) and Wei *et al.* (2022). Energy input (E_{in}) includes: Energy investment in preparation (E_1), Energy investment in drilling (E_2), Energy investment in drainage exploitation (E_3), Energy investment in Well-to-processing (WTP) transportation (E_4), Energy investment in processing (E_5), Energy investment in Processing-to-use (PTU) transportation (E_6), Energy investment in hydraulic fracturing (E_7) The ultimate gas recovery (UGR) in the life-cycle of a well E_{out} can be determined by the cumulative gas production and the heating value of natural gas (35.8 MJ/m^3). $EROI_{use}$ indicate EROI within the boundary from well to utilization:

$$EROI_{\mathrm{use}} = \frac{E_{out} - L_{\mathrm{a}} - L_{\mathrm{b}} - L_{\mathrm{c}}}{E_1 + E_2 + E_3 + E_4 + E_5 + E_6 + E_7} \tag{B-1}$$

where L_a is NGH losses during WTP transportation, L_b represents NGH losses during processing, L_c denotes NGH losses during PTU transportation.

$$E_1 = T\left(C_{\mathrm{platform}} EI + M_{\mathrm{diesel}} h_{\mathrm{diesel}}\right) \tag{B-2}$$

where $C_{platform}$ is the offshore platform investment for a well per year ($/yr), T refers to the life-cycle span of a well (yr), EI represents the energy intensity of an economy (MJ/$), M_{diesel} is the annual diesel consumption of a well (kg/yr), and h_{diesel} signifies the heating value of diesel (MJ/kg).

$$E_2 = R_{\mathrm{diesel}} T_{\mathrm{drilling}} h_{\mathrm{diesel}} + \left(C_{\mathrm{drilling}} - C_{\mathrm{diesel}}\right) EI \tag{B-3}$$

where R_{diesel} is the daily average diesel consumption (kg/day), $T_{drilling}$ symbolizes the drilling time (days), $C_{drilling}$ refers to the total drilling monetary cost ($), C_{diesel} denotes the cost of purchasing diesel ($), and d_{well} is the well depth (m). The value of $C_{\mathrm{drilling}} = 670 e^{0.005\mathrm{d}} d_{\mathrm{well}}$.

$$E_3 = M_{\mathrm{mater}} d_{\mathrm{well}} I_{\mathrm{pump}} M_{\mathrm{electric}} + M_{\mathrm{mater}} I_{\mathrm{disposal}} \tag{B-4}$$

where M_{water} is the amount of water (m^3), I_{pump} corresponds to the effective power of the electrical submersible pump (0.01 kWh/m^3·m), and $h_{electric}$ represents the heating value of electricity (MJ/kWh), $I_{disposal}$ is the unit energy consumption for water disposal (81.8 MJ/m^3).

$$E_4 = C_{\text{pipeline}} EI + M_{\text{transp}} D_{\text{transp}} I_{\text{transp}} \quad \text{(B-5)}$$

where $C_{pipeline}$ symbolizes the cost of pipeline construction ($), M_{transp} is the product of traffic volume (m^3), D_{transp} denotes transport distance (m), I_{transp} represents traffic intensity of gas pipeline (2.68 × 10^{-4} MJ/m^3·km).

$$E_5 = L_{\text{b}}/92\% \quad \text{(B-6)}$$

where L_b = 10%(E_{out}-L_a).

$$E_6 = C_{\text{pipeline}} EI + M_{\text{transp}} D_{\text{transp}} I_{\text{transp}} \quad \text{(B-7)}$$

where $C_{pipeline}$ refers to the cost of pipeline construction ($), M_{transp} symbolizes the product of traffic volume (m^3), D_{transp} is transport distance (m), I_{transp} represents traffic intensity of gas pipeline (2.68 × 10^{-4} MJ/m^3·km).

$$E_7 = E_{\text{pf}} + E_{\text{water}} + E_{\text{proppant}} + E_{\text{treat}} \quad \text{(B-8)}$$

$$E_{\text{pf}} = \frac{E_{\text{direct}}}{\eta_{\text{p}} \varepsilon_{\text{pg}}} \quad \text{(B-9)}$$

$$E_{\text{water}} = 50 Q_{\text{total}} \quad \text{(B-10)}$$

$$E_{\text{treat}} = 10\% Q_{\text{total}} I_{disposal} \quad \text{(B-11)}$$

Where E_{pf} is energy for pumping (MJ), η_p represents the efficiency of the pump, here = 0.6, ε_{pg} is the power generation energy efficiency, =0.4, E_{water} is water usage energy (MJ), $E_{proppant}$ refers to proppant usage energy (MJ), E_{treat} represents energy consumption for flowback fluid treatment (Balashov *et al.*, 2015), Q_{total} is Total estimated fluid injection volume (m^3), $I_{disposal}$ is the unit energy consumption for water disposal (81.8 MJ/m^3). It should be noted that the energy values for proppant usage are not explicitly formulated here, but are proportionally scaled based on the baseline

energy assessment results from the literature (Lior, 2016) according to the actual fluid injection volume designed in this study.

Goodfellow et al. (2015) showed that a substantial fraction of the injection energy is expended on deformation associated with fracture opening. Therefore, the total hydraulic injection energy is an appropriate measure of engineering energy input. According to Feng et al. (2019), the total hydraulic energy injected (E_{inj}) is defined as the time integral of the product of injection pressure and rate. The effective minimum horizontal stress in the Shenhu hydrate reservoir is only 0.5–0.9 MPa, indicating an extremely low effective stress regime in shallow marine hydrate sediments (Nie *et al.*, 2024). Under deepwater conditions, the hydrostatic pressure of the wellbore fluid is of the same order as the in-situ pore pressure. Therefore, the surface injection pressure can be reasonably approximated as the sum of the net pressure and friction pressure. Assuming a relatively constant bottom-hole injection pressure during the main fracturing treatment, the equation is simplified to:

$$E_{\mathrm{direct}} = (P_{\mathrm{friction}} + \sigma_{\mathrm{min}})Q_{\mathrm{total}} \tag{B-12}$$

Where P_{friction} denotes the pressure loss due to fluid friction along the wellbore (MPa), σ_{min} symbolizes the minimum horizontal principal stress (MPa), E_{direct} is the total hydraulic energy input during the fracturing process (MJ).

According to Ren *et al.* (2024), the pore volume of a single primary artificial fracture and the material balance equation for the fracturing fluid system as:

$$V_{\mathrm{f}} = 2x_{\mathrm{f}}w_{\mathrm{f}}H \tag{B-13}$$

$$Q_{\text{total}} = V_{\text{w}} + m(V_{\text{f}} + V_{\text{s}} + V_{\text{m}}) \quad \text{(B-14)}$$

In engineering estimation, accurately determining the secondary fracture volume (V_{s}) and matrix imbibition volume (V_{m}) a priori is challenging. However, Ren et al. (2024) demonstrated that matrix imbibition can account for a dominant proportion (e.g., 87.57%) of the total injected volume in tight reservoirs. To account for this without explicit micro-parameters, we introduced a Fluid Efficiency coefficient (η). The simplified formula used for estimation is:

$$Q_{\text{total}} \approx \frac{N_{\text{frac}} V_{\text{f}}}{\eta} = \frac{L_{\text{well}} V_{\text{f}}}{\eta d} \quad \text{(B-15)}$$

Where N_{frac} denotes total number of fractures, V_{f} refers to pore volume of a single primary fracture (m^3), H represents reservoir thickness (m), L_{well} represents the length of the horizontal production section (m), η is fluid efficiency factor. The value of $\eta = 0.1$.

Given the global target permeability (K_{target}), the fracture geometry is determined according to seepage mechanics. The drainage area controlled by the horizontal well is simplified into a series flow model consisting of two distinct zones: (a) The distal unstimulated matrix: length (x_{max} - x_{f}) with permeability K_{matrix}, and (b) The near-wellbore stimulated reservoir volume (SRV): Length x_{f} with enhanced permeability K_{SRV}.

According to the harmonic mean principle for flow perpendicular to the material interfaces in a heterogeneous formation, the relationship between the global target permeability and the zonal permeabilities is expressed as (Renard and Marsily, 1997):

$$\frac{x_{max}}{K_{\text{target}}} = \frac{x_{max}-x_{\text{f}}}{K_{\text{matrix}}} + \frac{x_{\text{f}}}{K_{\text{SRV}}} \tag{B-16}$$

$$K_{\text{SRV}} = \frac{K_{\text{matrix}}(d-w_{\text{f}})+K_{\text{f}}w_{\text{f}}}{d} \approx K_{\text{matrix}} + \frac{K_{\text{f}}w_{\text{f}}}{d} \tag{B-17}$$

The required fracture spacing is derived as:

$$d = \frac{K_{\text{f}}w_{\text{f}}}{K_{\text{SRV}}-K_{\text{matrix}}} \tag{B-18}$$

Among which x_{max} is drainage zone of horizontal well, roughly defined as the max recoverable zone (m), x_{f} represents fracture length (m), K_{target} denotes target global effective permeability (m^2), K_{matrix} symbolizes the intrinsic matrix permeability (m^2), K_{SRV} refers to the required equivalent permeability of the stimulated zone, d is fracture spacing along the horizontal wellbore (m), K_{f} represents fracture permeability (m^2), w_{f} denotes fracture width (m).

999 Table B-1 Detailed results of the EROI calculation process.

Site			GMGS6-SH02					
Case			1k	5k	10k	15k	20k	25k
drilling length (m)			9,496	3,876	2,835	2,445	2,244	2,119
Water depth (m)			1,225	1,225	1,225	1,225	1,225	1,225
Well depth (m)			10721.09	5,101	4,060	3,670	3,469	3,344
UGR of a single well (GJ)			26,134,000	26,134,000	26,134,000	26,134,000	26,134,000	26,134,000
Production period (years)			10	10	10	10	10	10
Water (10^7 m^3)			5.90	6.90	7 .18	7 .45	7.74	8.05
Energy cost (GJ)	Preparation E1	Platform investment	105,000	105,000	105,000	105,000	105,000	105,000
		Platform operation	168,046	168,046	168,046	168,046	168,046	168,046
	Drilling E2	Direct inputs	15,606	7,425	5,910	5,343	5,049	4,867
		Indirect inputs	1,147,280	258,666	165,404	135,959	121,890	113,539
	Drainage exploitation E3	Heating	0	0	0	0	0	0
		Drainage	22,780,383	12,663,122	10,494,098	9,844,860	9,667,049	9,689,300
		Water	4,828,062	5,640,754	5,873,072	6,094,741	6,332,357	6,584,730
	WTP Transportation E4	Leakage	784,020	784,020	784,020	784,020	784,020	784,020
		Direct inputs	68,474	68,474	68,474	68,474	68,474	68,474
		Indirect inputs	153,125	153,125	153,125	153,125	153,125	153,125
	Processing E5	Self-used energy	2,534,998	2,534,998	2,534,998	2,534,998	2,534,998	2,534,998
		Electricity input	220,435	220,435	220,435	220,435	220,435	220,435
	Processing-to-Use Transportation E6	Leakage	684,449	684,449	684,449	684,449	684,449	684,449
		Direct inputs	9,489	9,489	9,489	9,489	9,489	9,489
		Indirect inputs	21,875	21,875	21,875	21,875	21,875	21,875
	Hydraulic fracturing E7	Pumping	132,881	583,866	574,456	574,712	584,916	595,639
		Water	183,982	1,038,796	1,079,012	1,102,497	1,134,573	1,163,429
		Flowback treatment	30,099	169,947	176,526	180,368	185,616	190,337
		Proppant	8,831	49,862	51,793	52,920	54,460	55,845

1000

Appendix C

Regarding the impact of hydrate formation on gas production rate, we adopt the following formation model (Englezos *et al*., 1987; Sun and Mohanty, 2006; Gao *et al*., 2024):

$$R_r = -k_f A_s (p_e - p_G) \tag{C-1}$$

$$A_s = \sqrt{\frac{\phi_{wg}^{3\ 3}}{2K}} (S_L S_G S_H)^{2/3} \tag{C-2}$$

Among which: k_f = 0.5875×10^{-11} mol/(m^2·MPa•s), S_w means liquid saturation, S_G is gas saturation, S_H represents hydrate saturation, P_e denotes hydrate phase equilibrium pressure (Pa), P_G is gas pressure (Pa), ϕ_{wg} refers to effective porosity, K is intrinsic permeability (m^2).

To support the reliability of the numerical simulations, this appendix presents a supplementary evaluation of the model's robustness and theoretical premises. A sensitivity analysis on key parameters—including thermodynamic properties and hydrate dissociation kinetics—is conducted to assess their impacts on gas production.

To evaluate the robustness of the proposed analytical model against the assumption of horizontally dominated flow, validation for its applicability under anisotropic permeability conditions was conducted. In this context, anisotropy refers specifically to the contrast between horizontal and vertical intrinsic permeability. We conducted a series of numerical simulations with a fixed vertical intrinsic permeability (k_{hbs_v} = 2.38 mD), while varying the ratio of horizontal to vertical permeability (R_{hv}) from 0.1 to 10. As illustrated in Fig. C-3(a), the production range predicted by the analytical method remains in good agreement with the numerical solutions across this entire range. These

results demonstrate that the proposed method maintains satisfactory accuracy and robustness even under moderately to strongly anisotropic conditions. While currently focused on a single-well model, the framework could be extended to multi-well scenarios (Terzariol and Santamarina, 2021). Preliminary validation against numerical simulations shows an error of less than 10% (Fig. C-3(b)); however, comprehensive research on multi-well interference is reserved for future work.

References

(1) Sloan, E. D., Jr.; Koh, C. A. *Clathrate Hydrates of Natural Gases*, 3rd ed.; CRC Press: Boca Raton, FL, **2007**. DOI: 10.1201/9781420008494.

(2) Moridis, G. J.; Silpngarmlert, S.; Reagan, M. T.; Collett, T.; Zhang, K. Gas production from a cold, stratigraphically-bounded gas hydrate deposit at the Mount Elbert Gas Hydrate Stratigraphic Test Well, Alaska North Slope: Implications of uncertainties. *Mar. Pet. Geol.* **2011**, *28* (2), 517–534. DOI: 10.1016/j.marpetgeo.2010.01.005.

(3) Dong, L.; Wu, N.; Liu, F.; Sun, Z.; Qi, M.; Hu, G.; Li, Y. Estimation on strength parameters of sediments with hydrate layered distribution based on triaxial shearing tests. *Gas Sci. Eng.* **2024**, *123*, 205255. DOI: 10.1016/j.jgsce.2024.205255.

(4) Li, B.; Liang, Y.-P.; Li, X.-S.; Zhou, L. A pilot-scale study of gas production from hydrate deposits with two-spot horizontal well system. *Appl. Energy* **2016**, *176*, 12–21. DOI: 10.1016/j.apenergy.2016.05.061.

(5) Yamamoto, K.; Terao, Y.; Fujii, T.; Ikawa, T.; Seki, M.; Matsuzawa, M.; Kanno, T. Operational overview of the first offshore production test of methane hydrates in the Eastern Nankai Trough. In *Offshore Technology Conference*; OTC: Houston, Texas, **2014**. DOI: 10.4043/25243-MS.

(6) Yamamoto, K.; Wang, X.-X.; Tamaki, M.; Suzuki, K. The second offshore production of methane hydrate in the Nankai Trough and gas production behavior from a heterogeneous methane hydrate reservoir. *RSC Adv.* **2019**, *9* (45), 25987–26013. DOI: 10.1039/C9RA00755E.

(7) Ye, J.; Qin, X.; Qiu, H.; Xie, W.; Lu, H.; Lu, C.; Zhou, J.; Liu, J.; Yang, T.; Cao, J.; et al. Data report: Molecular and isotopic compositions of the extracted gas from China's first offshore natural gas hydrate production test in South China Sea. *Energies* **2018**, *11* (10), 2793. DOI: 10.3390/en11102793.

(8) Ye, J.; Qin, X.; Xie, W.; Lu, H.; Ma, B.; Qiu, H.; Liang, J.; Lu, J.; Kuang, Z.; Lu, C.; et al. The second natural gas hydrate production test in the South China Sea. *China Geol.* **2020**, *3* (2), 197–209. DOI: 10.31035/cg2020043.

(9) Moridis, G. J.; Collett, T. S.; Boswell, R.; Kurihara, M.; Reagan, M. T.; Koh, C.; Sloan, E. D. Toward production from gas hydrates: Current status, assessment of resources, and simulation-

based evaluation of technology and potential. *SPE Res. Eval. Eng.* **2009**, *12* (05), 745–771. DOI: 10.2118/114163-PA.

(10) Feng, Y.; Chen, L.; Suzuki, A.; Kogawa, T.; Okajima, J.; Komiya, A.; Maruyama, S. Numerical analysis of gas production from layered methane hydrate reservoirs by depressurization. *Energy* **2019**, *166*, 1106–1119. DOI: 10.1016/j.energy.2018.10.184.

(11) Zhao, L.; Fan, Z.; Li, M.; Li, P.; Wang, D. Unraveling the complex pressure propagation of two-time depressurization production in Shenhu hydrate reservoir: Insights for long-term exploitation. *Gas Sci. Eng.* **2023**, *119*, 205142. DOI: 10.1016/j.jgsce.2023.205142.

(12) Wu, N.; Li, Y.; Wan, Y.; Sun, J.; Huang, L.; Mao, P. Prospect of marine natural gas hydrate stimulation theory and technology system. *Nat. Gas Ind. B* **2021**, *8* (2), 173–187. DOI: 10.1016/j.ngib.2020.08.003.

(13) Pang, W. X.; Li, Q. P.; Zhou, S. W. Research and development strategy of natural gas hydrate development. *Int. Pet. Econ.* **2022**, *30* (12), 33–41 (in Chinese).

(14) Wu, L.; Zhang, T.; Zhang, H.; Sui, Y.; Yu, X.; Miao, M. Economic evaluation of production capacity for natural gas hydrate industrial exploitation in the South China Sea. *Front. Earth Sci.* **2022**, *10*, 990562. DOI: 10.3389/feart.2022.990562.

(15) Li, S.; Wu, D.; Wang, X.; Hao, Y. Enhanced gas production from marine hydrate reservoirs by hydraulic fracturing assisted with sealing burdens. *Energy* **2021**, *232*, 120889. DOI: 10.1016/j.energy.2021.120889.

(16) Lv, T.; Cai, J.; Ding, Y.; Pan, J.; Chen, Z.; Li, X. Numerical evaluation of long-term depressurization production of a multilayer gas hydrate reservoir and its hydraulic fracturing applications. *Energy Fuels* **2022**, *36* (6), 3154–3168. DOI: 10.1021/acs.energyfuels.1c04017.

(17) Wei, R.; Xia, Y.; Wang, Z.; Li, Q.; Lv, X.; Leng, S.; Zhang, L.; Zhang, Y.; Xiao, B.; Yang, S.; et al. Long-term numerical simulation of a joint production of gas hydrate and underlying shallow gas through dual horizontal wells in the South China Sea. *Appl. Energy* **2022**, *320*, 119235. DOI: 10.1016/j.apenergy.2022.119235.

(18) Cheng, F.; Sun, X.; Li, Y.; Ju, X.; Yang, Y.; Liu, X.; Liu, W.; Yang, M.; Song, Y. Numerical analysis of coupled thermal-hydro-chemo-mechanical (THCM) behavior to joint production of

marine gas hydrate and shallow gas. *Energy* **2023**, *281*, 128224. DOI: 10.1016/j.energy.2023.128224.

(19) Ge, K.; Liu, J.; Wang, J.; Long, Z.; Zhang, X.; Wei, H.; Yu, W. Numerical simulation of gas production behavior of Class I, Class II and Class III hydrate reservoirs for different well locations. *J. Cleaner Prod.* **2023**, *433*, 139844. DOI: 10.1016/j.jclepro.2023.139844.

(20) Sun, J.; Gu, Y.; Yin, Z.; Zhao, Y.; Ning, F. Production performance of multiple approaches for stimulating the layered hydrate reservoir with high permeability under horizontal well systems. *Ocean Eng.* **2024**, *303*, 117781. DOI: 10.1016/j.oceaneng.2024.117781.

(21) Qin, F.; Sun, J.; Cao, X.; Mao, P.; Zhang, L.; Lei, G.; Jiang, G.; Ning, F. Numerical simulation on combined production of hydrate and free gas from silty clay reservoir in the South China Sea by depressurization: Formation sealing. *Appl. Energy* **2025**, *377*, 124343. DOI: 10.1016/j.apenergy.2024.124343.

(22) Ye, H.; Zhang, Q.; Yao, Y.; Duan, J.; Chen, D.; Lu, H.; Wu, X.; Li, D.; Jiang, Y.; Zi, M. Co-production of gas hydrates, shallow gas, and deep gas in the Qiongdongnan Basin: A pathway to commercial production. *Appl. Energy* **2025**, *384*, 125482. DOI: 10.1016/j.apenergy.2025.125482.

(23) Yu, T.; Guan, G.; Wang, D.; Song, Y.; Abudula, A. Numerical evaluation on the effect of horizontal-well systems on the long-term gas hydrate production behavior at the second Shenhu test site. *J. Nat. Gas Sci. Eng.* **2021**, *95*, 104200. DOI: 10.1016/j.jngse.2021.104200.

(24) Shang, S.; Gu, L.; Zhan, L.; Lu, H. Numerical study of the effect of thermal stimulation on gas production from marine hydrate reservoirs. *Energy Fuels* **2022**, *36* (16), 9036–9047. DOI: 10.1021/acs.energyfuels.2c01257.

(25) Fan, S.; Wang, Y.; Wang, H.; Zhang, X.; Zhu, Y.; Che, J.; Sun, B.; Yang, N.; Yang, C.; Xu, H.; et al. Enhancing gas production from methane hydrate decomposition by microwave heating-induced: Modeling and experimental validation. *Energy* **2025**, *322*, 135566. DOI: 10.1016/j.energy.2025.135566.

(26) Zhang, X.; Guan, Y.; Yue, C.; Sun, Z.; Guo, H.; Zhang, Y.; Wang, D.; Wang, Y. Multiphysics modeling of synergistic microwave heating and nitrogen injection for methane hydrate

recovery. *Fuel* **2026**, *410*, 137880. DOI: 10.1016/j.fuel.2025.137880.

(27) Kan, J.-Y.; Sun, Y.-F.; Yang, J.-H.; Han, Z.; Rao, D.; Li, N.; Li, Z.; Chen, G.-J. Numerical study on gas recovery and escape during gas hydrate exploitation enhanced by continuous CO2/H2 injection. *Energy Fuels* **2025**, *39* (3), 1615–1627. DOI: 10.1021/acs.energyfuels.4c05530.

(28) Zhong, X.; Pan, D.; Zhu, Y.; Wang, Y.; Zhai, L.; Li, X.; Tu, G.; Chen, C. Fracture network stimulation effect on hydrate development by depressurization combined with thermal stimulation using injection-production well patterns. *Energy* **2021**, *228*, 120601. DOI: 10.1016/j.energy.2021.120601.

(29) Mao, P.; Wu, N.; Wan, Y.; Hu, G.; Wang, X. Optimization of a multi-fractured multilateral well network in advantageous structural positions of ultralow-permeability hydrate reservoirs. *Energy* **2023**, *268*, 126623. DOI: 10.1016/j.energy.2023.126623.

(30) Zhang, Z.; Xu, T.; Li, S.; He, J.; Li, X.; Li, Y.; Lu, C.; Qin, X. Optimizing fracturing techniques for enhanced hydrate dissociation in low-permeability reservoirs: Insights from numerical simulation. *Gas Sci. Eng.* **2024**, *125*, 205309. DOI: 10.1016/j.jgsce.2024.205309.

(31) Li, P.; Fan, Z.; Zhao, L.; Yang, C.; He, K.; Wang, D. Underestimated risks for application of hydraulic fracturing into hydrate exploitation: In the perspective of formation deformation and sand production. *Mar. Pet. Geol.* **2025**, *177*, 107393. DOI: 10.1016/j.marpetgeo.2025.107393.

(32) Sun, J.; Ning, F.; Liu, T.; Liu, C.; Chen, Q.; Li, Y.; Cao, X.; Mao, P.; Zhang, L.; Jiang, G. Gas production from a silty hydrate reservoir in the South China Sea using hydraulic fracturing: A numerical simulation. *Energy Sci. Eng.* **2019**, *7* (4), 1106–1122. DOI: 10.1002/ese3.353.

(33) Mu, Z.; Yan, Z.; Qiu, Z.; Zhang, P.; Zhang, Y.; Tian, S.; Zhang, B. Impact of fracture orientation on gas hydrate extraction using horizontal well depressurization and hydraulic fracturing. *Energy* **2025**, *315*, 134367. DOI: 10.1016/j.energy.2025.134367.

(34) Xu, J.; Sun, W.; Li, H.; Li, S. Simulation of production dynamics after reservoir stimulation in hydrate reservoirs considering complex fracture morphology. *Energy Fuels* **2023**, *37* (18), 13866–13879. DOI: 10.1021/acs.energyfuels.3c02249.

(35) Huang, Y.; Wang, T.; Wang, R.; Wang, H.; Lu, X.; Zhang, X. Numerical simulation of hydraulic fracture characteristics in gas hydrate bearing-sediments by using CDEM. *Acta Mech. Sin.*

2024, *40* (2), 322273. DOI: 10.1007/s10409-023-23273-x.

(36) Cheng, F.; Lyu, H.; Liu, W.; Sun, X.; You, Z.; Li, Y.; Tian, Y. Modeling fracture propagation in hydrate bearing sediments using phase field method. *Comput. Geotech.* **2025**, *188*, 107532. DOI: 10.1016/j.compgeo.2025.107532.

(37) Terzariol, M.; Goldsztein, G.; Santamarina, J. C. Maximum recoverable gas from hydrate bearing sediments by depressurization. *Energy* **2017**, *141*, 1622–1628. DOI: 10.1016/j.energy.2017.11.076.

(38) Terzariol, M.; Santamarina, J. C. Multi-well strategy for gas production by depressurization from methane hydrate-bearing sediments. *Energy* **2021**, *220*, 119710. DOI: 10.1016/j.energy.2020.119710.

(39) Lu, N.; Hou, J.; Liu, Y.; Barrufet, M. A.; Ji, Y.; Xia, Z.; Xu, B. Stage analysis and production evaluation for Class III gas hydrate deposit by depressurization. *Energy* **2018**, *165*, 501–511. DOI: 10.1016/j.energy.2018.09.184.

(40) Zhang, B.; Jiang, R.; Sun, B.; Lu, N.; Hou, J.; Bai, Y.; Chen, W.; Liu, Y. Establishment of the productivity prediction method of Class III gas hydrate developed by depressurization and horizontal well based on production performance and inflow relationship. *Fuel* **2022**, *308*, 122006. DOI: 10.1016/j.fuel.2021.122006.

(41) Yang, M.; Fu, Z.; Zhao, Y.; Jiang, L.; Zhao, J.; Song, Y. Effect of depressurization pressure on methane recovery from hydrate–gas–water bearing sediments. *Fuel* **2016**, *166*, 419–426. DOI: 10.1016/j.fuel.2015.10.119.

(42) Cheng, F.; Liu, W.; Lv, H.; Sun, X.; Wu, P.; Li, Y. Impact of varied depressurization rates on gas production and heat supply in hydrate dissociation. *Energy Fuels* **2024**, *38* (11), 9734–9741. DOI: 10.1021/acs.energyfuels.4c01343.

(43) Sanavia, L.; Pesavento, F.; Schrefler, B. A. Finite element analysis of non-isothermal multiphase geomaterials with application to strain localization simulation. *Comput. Mech.* **2006**, *37* (4), 331. DOI: 10.1007/s00466-005-0673-6.

(44) Teymouri, M.; Sánchez, M.; Santamarina, J. C. A pseudo-kinetic model to simulate phase changes in gas hydrate bearing sediments. *Mar. Pet. Geol.* **2020**, *120*, 104519. DOI:

10.1016/j.marpetgeo.2020.104519.

(45) Gamwo, I. K.; Liu, Y. Mathematical modeling and numerical simulation of methane production in a hydrate reservoir. *Ind. Eng. Chem. Res.* **2010**, *49* (11), 5231–5245. DOI: 10.1021/ie901452v.

(46) Liao, Y.; Zheng, J.; Wang, Z.; Sun, B.; Sun, X.; Linga, P. Modeling and characterizing the thermal and kinetic behavior of methane hydrate dissociation in sandy porous media. *Appl. Energy* **2022**, *312*, 118804. DOI: 10.1016/j.apenergy.2022.118804.

(47) Shan, Z.; Zhou, B.; Kong, Q.; Wang, X.; Liao, Y.; Wang, Z.; Zhang, J. Analysis of production laws of hydrate reservoirs via combined heat injection and depressurization based on local thermal non-equilibrium. *J. Mar. Sci. Eng.* **2024**, *12* (8), 1408. DOI: 10.3390/jmse12081408.

(48) White, M. D.; Kneafsey, T. J.; Seol, Y.; Waite, W. F.; Uchida, S.; Lin, J. S.; Myshakin, E. M.; Gai, X.; Gupta, S.; Reagan, M. T.; et al. An international code comparison study on coupled thermal, hydrologic and geomechanical processes of natural gas hydrate-bearing sediments. *Mar. Pet. Geol.* **2020**, *120*, 104566. DOI: 10.1016/j.marpetgeo.2020.104566.

(49) Kowalsky, M. B.; Moridis, G. J. Comparison of kinetic and equilibrium reaction models in simulating gas hydrate behavior in porous media. *Energy Convers. Manage.* **2007**, *48* (6), 1850–1863. DOI: 10.1016/j.enconman.2007.01.017.

(50) Sánchez, M.; Santamarina, C.; Teymouri, M.; Gai, X. Coupled numerical modeling of gas hydrate-bearing sediments: From laboratory to field-scale analyses. *J. Geophys. Res.: Solid Earth* **2018**, *123* (12). DOI: 10.1029/2018JB015966.

(51) Kim, H. C.; Bishnoi, P. R.; Heidemann, R. A.; Rizvi, S. S. H. Kinetics of methane hydrate decomposition. *Chem. Eng. Sci.* **1987**, *42* (7), 1645–1653. DOI: 10.1016/0009-2509(87)80169-0.

(52) Ye, Z.; Wang, L.; Zhu, B.; Shao, H.; Xu, W.; Chen, Y. A thermo-hydro-chemo-mechanical coupled model for natural gas hydrate-bearing sediments considering gravity effect. *J. Nat. Gas Sci. Eng.* **2022**, *108*, 104823. DOI: 10.1016/j.jngse.2022.104823.

(53) Kolditz, O.; Bauer, S.; Bilke, L.; Böttcher, N.; Delfs, J. O.; Fischer, T.; Görke, U. J.; Kalbacher, T.; Kosakowski, G.; McDermott, C. I.; et al. OpenGeoSys: An open-source initiative for

numerical simulation of thermo-hydro-mechanical/chemical (THM/C) processes in porous media. *Environ. Earth Sci.* **2012**, *67* (2), 589–599. DOI: 10.1007/s12665-012-1546-x.

(54) Bilke, L.; Flemisch, B.; Kalbacher, T.; Kolditz, O.; Helmig, R.; Nagel, T. Development of open-source porous media simulators: Principles and experiences. *Transp. Porous Media* **2019**, *130* (1), 337–361. DOI: 10.1007/s11242-019-01310-1.

(55) Ye, Z. G.; Wang, L. J.; Zhu, B.; Chen, Y. M. Thermo-hydro-mechanical coupling model for natural gas hydrate-bearing sediments with depressurization based on OpenGeoSys. *Rock Soil Mech.* **2023**, *44* (11), 3191–3202. DOI: 10.16285/j.rsm.2023.1012.

(56) Schrefler, B. A.; Zhan, X.; Simoni, L. A coupled model for water flow, airflow and heat flow in deformable porous media. *Int. J. Numer. Methods Heat Fluid Flow* **1995**, *5* (6), 531–547. DOI: 10.1108/EUM0000000004077.

(57) Masuda, Y.; Fujinaga, Y.; Naganawa, S.; Fujita, K.; Sato, K.; Hayashi, Y. Modeling and experimental studies on dissociation of methane gas hydrates in Berea sandstone cores. In *Proceedings of the 3rd International Conference on Gas Hydrates*, Salt Lake City, UT, **1999**.

(58) Wang, X.; Sun, Y.; Li, B.; Zhang, G.; Guo, W.; Li, S.; Jiang, S.; Peng, S.; Chen, H. Reservoir stimulation of marine natural gas hydrate—A review. *Energy* **2023**, *263*, 126120. DOI: 10.1016/j.energy.2022.126120.

(59) Van Genuchten, M. Th. A closed-form equation for predicting the hydraulic conductivity of unsaturated soils. *Soil Sci. Soc. Am. J.* **1980**, *44* (5), 892–898. DOI: 10.2136/sssaj1980.03615995004400050002x.

(60) Moridis, G. J.; Seol, Y.; Kneafsey, T. J. *Studies of Reaction Kinetics of Methane Hydrate Dissociation in Porous Media*; Lawrence Berkeley National Laboratory: Berkeley, CA, **2005**. https://escholarship.org/uc/item/8q50w5cn.

(61) Moridis, G. J.; Kowalsky, M. B.; Pruess, K. Depressurization-induced gas production from Class 1 hydrate deposits. *SPE Res. Eval. Eng.* **2007**, *10* (5), 458–481. DOI: 10.2118/97266-PA.

(62) Li, G.; Wu, D.-M.; Li, X.-S.; Lv, Q.-N.; Li, C.; Zhang, Y. Experimental measurement and mathematical model of permeability with methane hydrate in quartz sands. *Appl. Energy* **2017**, *202*, 282–292. DOI: 10.1016/j.apenergy.2017.05.147.

(63) Li, Z. D.; Zhang, H. X.; Liu, S. F.; et al. *Basic Theory and Technology of Waterflooding Oilfield Development*; Science Press: Beijing, **2019** (in Chinese).

(64) Ye, Z.; Wang, L.; Zhu, B.; Yuan, S.; Yan, B.; Guo, R.; Chen, Y. A decomposition–consolidation model for the production behavior of gas hydrate-bearing sediments. *Int. J. Numer. Anal. Methods Geomech.* **2025**, *49* (8), 1913–1930. DOI: 10.1002/nag.3965.

(65) Xiao, C.-W.; Li, X.-S.; Li, G.; Yu, Y.; Yu, J.-X.; Lv, Q.-N. Numerical analysis of production behaviors and permeability characteristics on the second gas hydrate production test in the South China Sea. *Energy Fuels* **2022**, *36* (18), 10960–10974. DOI: 10.1021/acs.energyfuels.2c02385.

(66) Yin, F.; Gao, Y.; Zhang, H.; Sun, B.; Chen, Y.; Gao, D.; Zhao, X. Comprehensive evaluation of gas production efficiency and reservoir stability of horizontal well with different depressurization methods in low permeability hydrate reservoir. *Energy* **2022**, *239*, 122422. DOI: 10.1016/j.energy.2021.122422.

(67) Lior, N. Exergy, energy, and gas flow analysis of hydrofractured shale gas extraction. *J. Energy Resour. Technol.* **2016**, *138* (6), 061601. DOI: 10.1115/1.4032240.

(68) Kong, Z.; Jiang, Q.; Dong, X.; Wang, J.; Wan, X. Estimation of China's production efficiency of natural gas hydrates in the South China Sea. *J. Cleaner Prod.* **2018**, *203*, 1–12. DOI: 10.1016/j.jclepro.2018.08.262.

(69) Song, Y.; Cheng, C.; Zhao, J.; Zhu, Z.; Liu, W.; Yang, M.; Xue, K. Evaluation of gas production from methane hydrates using depressurization, thermal stimulation and combined methods. *Appl. Energy* **2015**, *145*, 265–277. DOI: 10.1016/j.apenergy.2015.02.040.

(70) Kou, X.; Wang, Y.; Li, X.-S.; Zhang, Y.; Chen, Z.-Y. Influence of heat conduction and heat convection on hydrate dissociation by depressurization in a pilot-scale hydrate simulator. *Appl. Energy* **2019**, *251*, 113405. DOI: 10.1016/j.apenergy.2019.113405.

(71) Zhao, J.; Xu, L.; Guo, X.; Li, Q.; Lv, X.; Fan, Q.; Zhao, J.; Dong, H.; Wang, B.; Yang, L. Enhancing the gas production efficiency of depressurization-induced methane hydrate exploitation via fracturing. *Fuel* **2021**, *288*, 119740. DOI: 10.1016/j.fuel.2020.119740.

(72) Moridis, G. J.; Reagan, M. T.; Zhang, K. The use of horizontal wells in gas production from

hydrate accumulations. In *Offshore Technology Conference*; OTC: Houston, TX, **2007**.

(73) Cipolla, C. L.; Warpinski, N. R.; Mayerhofer, M. J.; Lolon, E. P.; Vincent, M. C. The relationship between fracture complexity, reservoir properties, and fracture treatment design. In *SPE Annual Technical Conference and Exhibition*; SPE: Denver, CO, **2008**. DOI: 10.2118/115769-MS.

(74) Qi, Y.; Sun, Y.-H.; Li, B.; Shan, H.-F.; Liu, Y.-Z.; Zhang, G.-B. Novel dual-enhanced stimulation for safe and efficient marine hydrate production. *Pet. Sci.* **2025**, *22* (2), 805–820. DOI: 10.1016/j.petsci.2024.11.010.

(75) Balashov, V. N.; Engelder, T.; Gu, X.; Fantle, M. S.; Brantley, S. L. A model describing flowback chemistry changes with time after Marcellus Shale hydraulic fracturing. *AAPG Bull.* **2015**, *99* (1), 143–154. DOI: 10.1306/06041413119.

(76) Goodfellow, S. D.; Nasseri, M. H. B.; Maxwell, S. C.; Young, R. P. Hydraulic fracture energy budget: Insights from the laboratory. *Geophys. Res. Lett.* **2015**, *42* (9), 3179–3187. DOI: 10.1002/2015GL063093.

(77) Nie, S.; Liu, K.; Zhong, X.; Wang, Y.; Yang, B.; Song, J. Research on hydraulic fracture propagation patterns in multilayered gas hydrate reservoirs using a three-dimensional XFEM-based cohesive zone method. *Energy Fuels* **2024**, *38* (6), 5106–5123. DOI: 10.1021/acs.energyfuels.3c05015.

(78) Ren, L.; Dou, M.; Dong, X.; Chen, B.; Zhang, L.; Sun, J.; Jing, C.; Zhang, W.; Zhou, D.; Li, H. Quantitative characterization of stimulated reservoir volume (SRV) fracturing effects in naturally fractured unconventional hydrocarbon reservoirs. *Front. Earth Sci.* **2024**, *12*, 1419631. DOI: 10.3389/feart.2024.1419631.

(79) Renard, P.; de Marsily, G. Calculating equivalent permeability: A review. *Adv. Water Resour.* **1997**, *20* (5–6), 253–278. DOI: 10.1016/S0309-1708(96)00050-4.

(80) Englezos, P.; Kalogerakis, N.; Dholabhai, P. D.; Bishnoi, P. R. Kinetics of formation of methane and ethane gas hydrates. *Chem. Eng. Sci.* **1987**, *42* (11), 2647–2658. DOI: 10.1016/0009-2509(87)87015-X.

(81) Sun, X.; Mohanty, K. K. Kinetic simulation of methane hydrate formation and dissociation in

porous media. *Chem. Eng. Sci.* **2006**, *61* (11), 3476–3495. DOI: 10.1016/j.ces.2005.12.017.

(82) Gao, F.; Zhang, Y.; Chen, C.; Li, X.; Chen, Z. Numerical simulation of hydrate dissociation behaviors in hydrate reservoir with different properties during horizontal well drilling. *J. Mar. Sci. Eng.* **2024**, *12* (4), 554. DOI: 10.3390/jmse12040554.

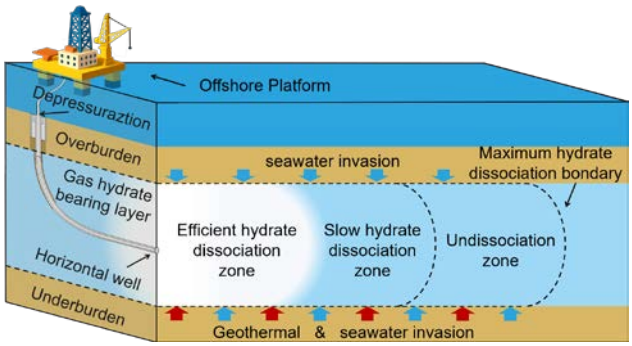
Offshore Platform
Depressuraztion
Overburden
Gas hydrate bearing layer
Horizontal well
Underburden
seawater invasion
Maximum hydrate dissociation bondary
Efficient hydrate dissociation zone
Slow hydrate dissociation zone
Undissociation zone
Geothermal & seawater invasion

TOC Graphic

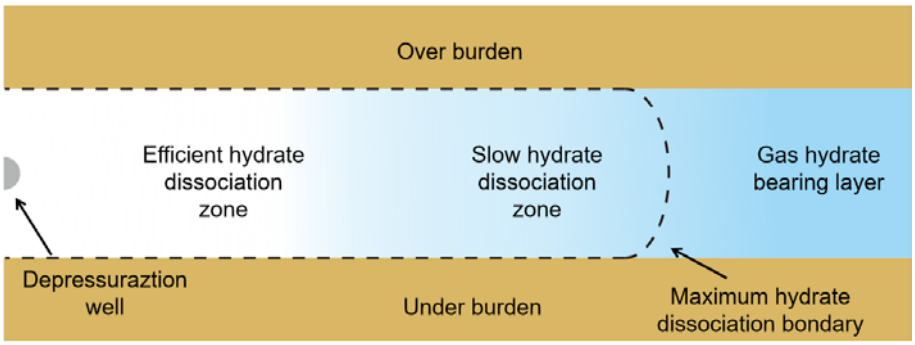

Fig. 1 Schematic diagram of the maximum recoverable zone and high-efficiency production zone in horizontal well depressurization.

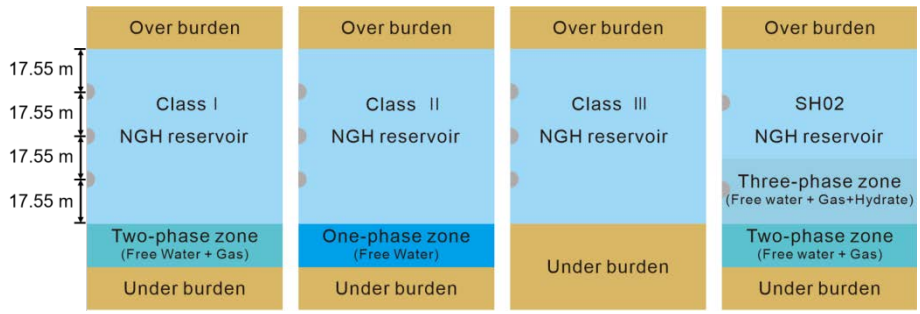

Fig. 2 Schematic diagrams of the three representative reservoir types and model for the Shenhu area.

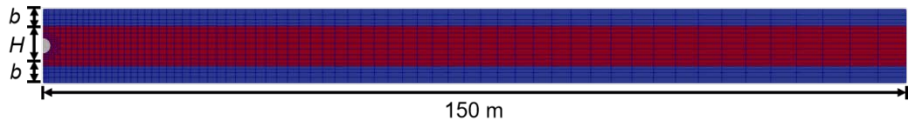

Fig. 3 Geometry and mesh attribute scheme of the numerical model used for validating the analytical solution.

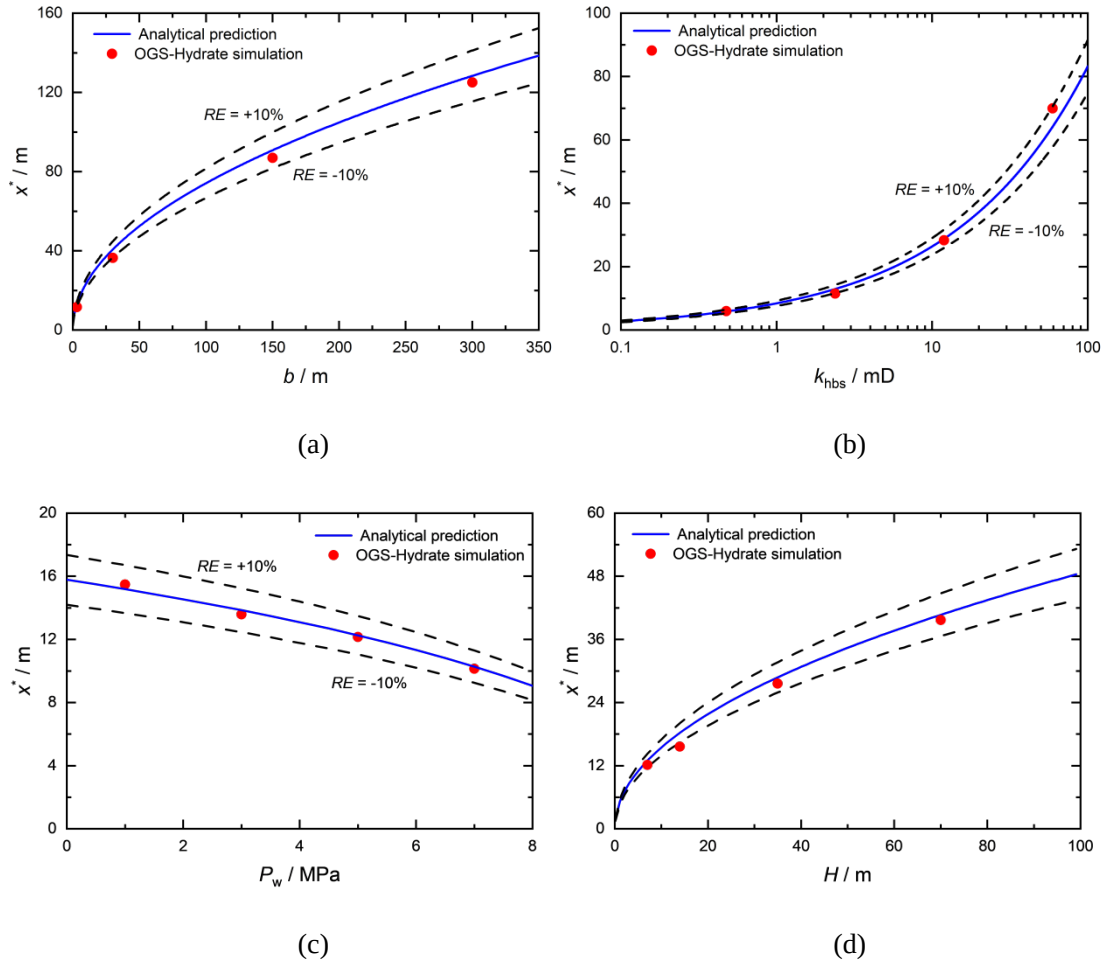

Fig. 4 Comparison of analytical solution predictions and numerical simulation results under different: (a) burden thickness b; (b) hydrate-bearing sediment permeability k_{hbs}; (c) pressure at the well P_w; (d) hydrate-bearing sediment thickness H.

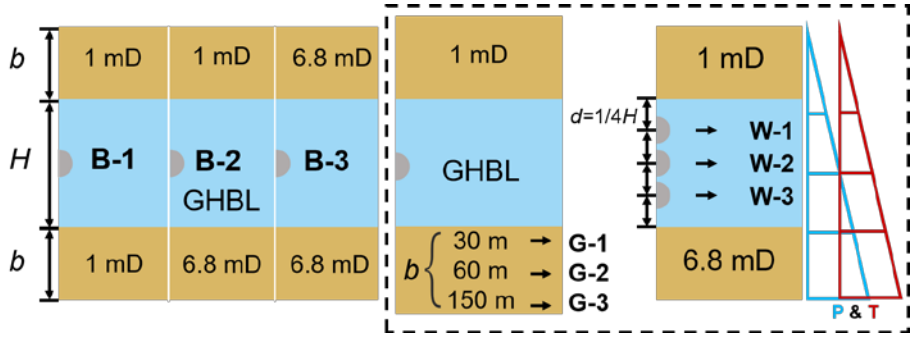

Fig. 5 Schematic of simulation scenarios designed to investigate the effects of burden properties (Run_B), thermal and pressure gradients (Run_G), and horizontal well configurations (Run_W).

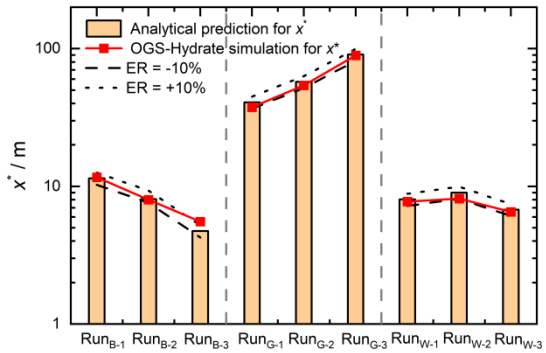

Fig. 6 Validation of the stratified weighted average method against numerical simulation results across different scenarios.

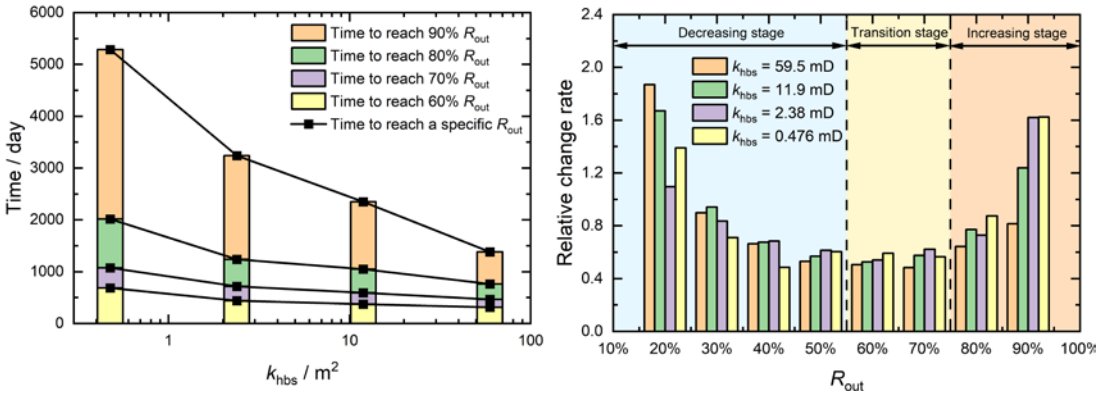

(a) (b)

Fig. 7 Evaluation of production efficiency indicators under different intrinsic permeabilities: (a) time required to reach specific recovery factor (R_{out}); (b) relative change rate of time for R_{out}.

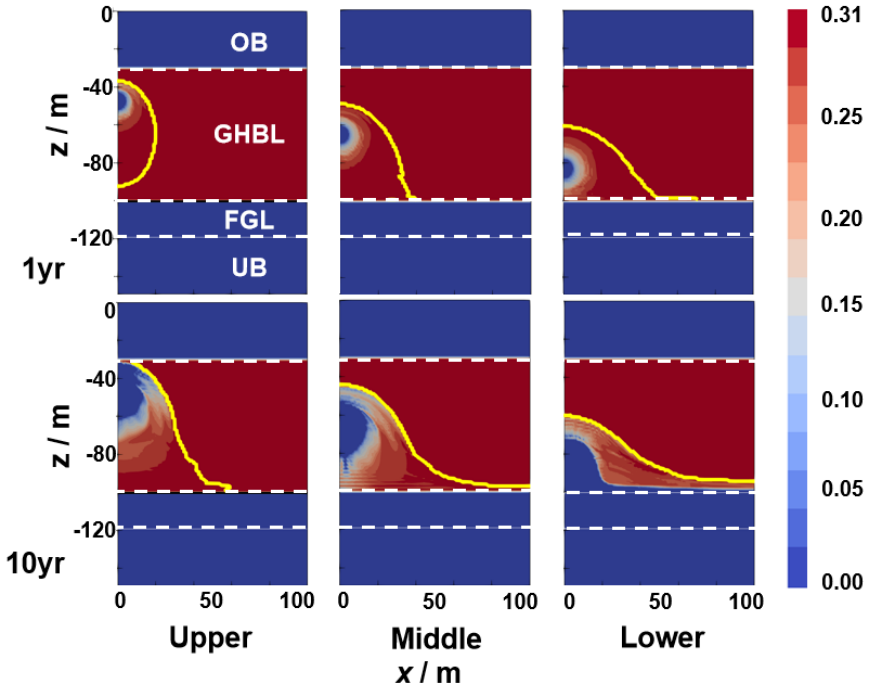
OB
GHBL
FGL
UB
1yr
10yr
z / m
0
-40
-80
-120
0
50
100
Upper
Middle
Lower
x / m
0.31
0.25
0.20
0.15
0.10
0.05
0.00

(a)

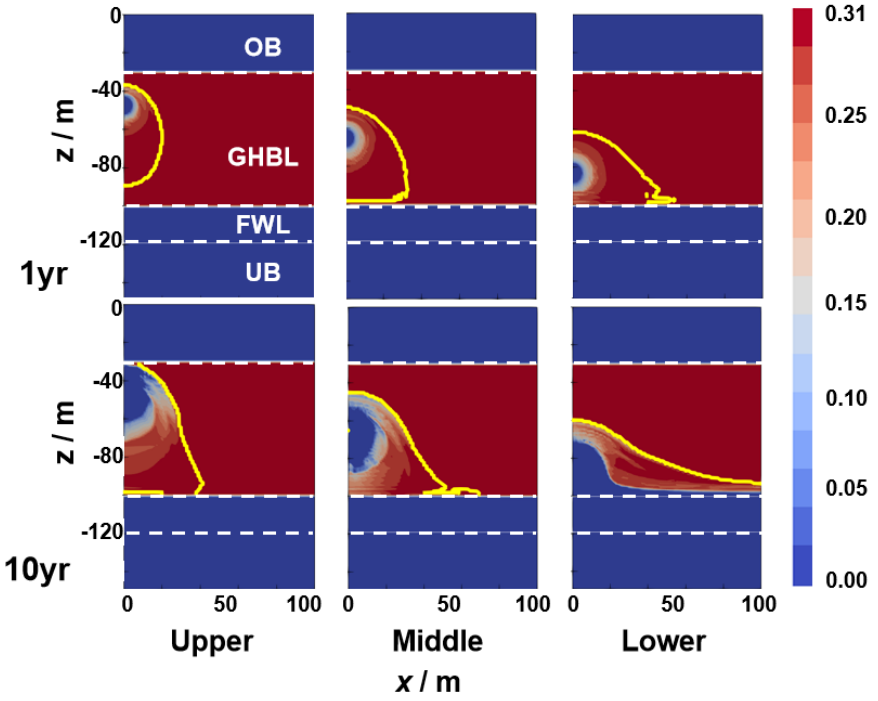

(b)

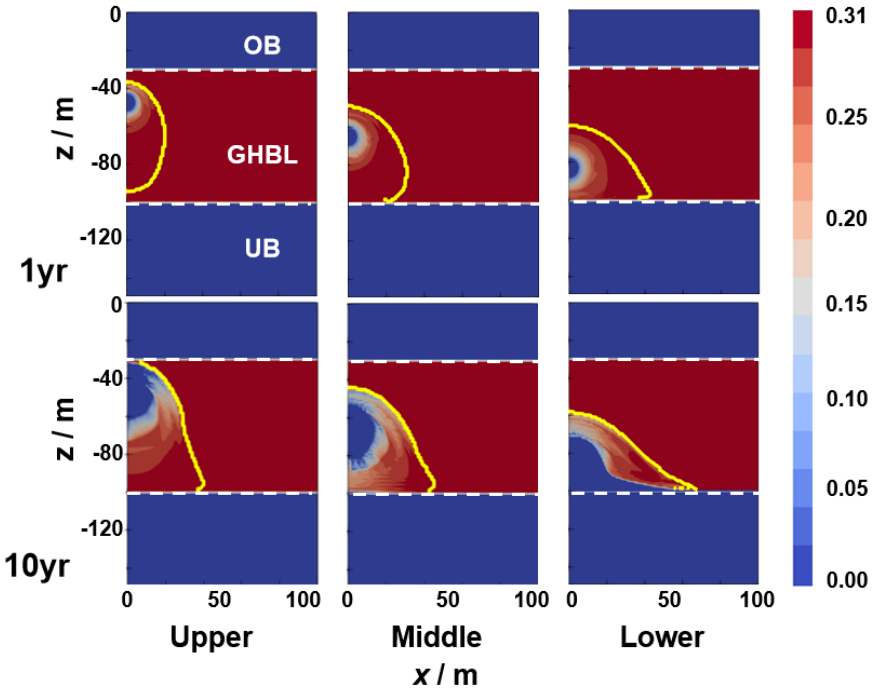

(c)

Fig. 8 Spatial distribution of hydrate saturation at 1 year and 10 years under different horizontal well configurations in: (a) Class I; (b) Class II; (c) Class III.

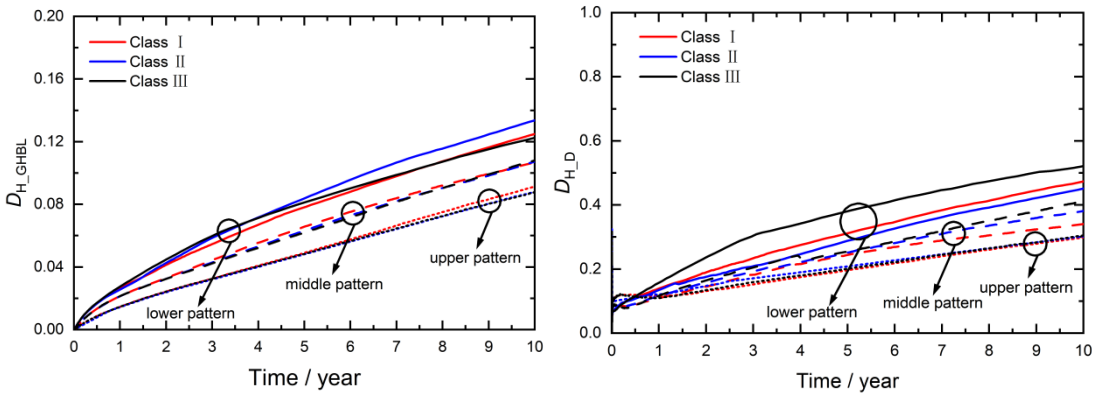

(a) (b)

Fig. 9 Evolution of the hydrate dissociation degrees: (a) in the GHBL (D_{H_GHBL}); (b) in the dissociation zone (D_{H_D}).

122

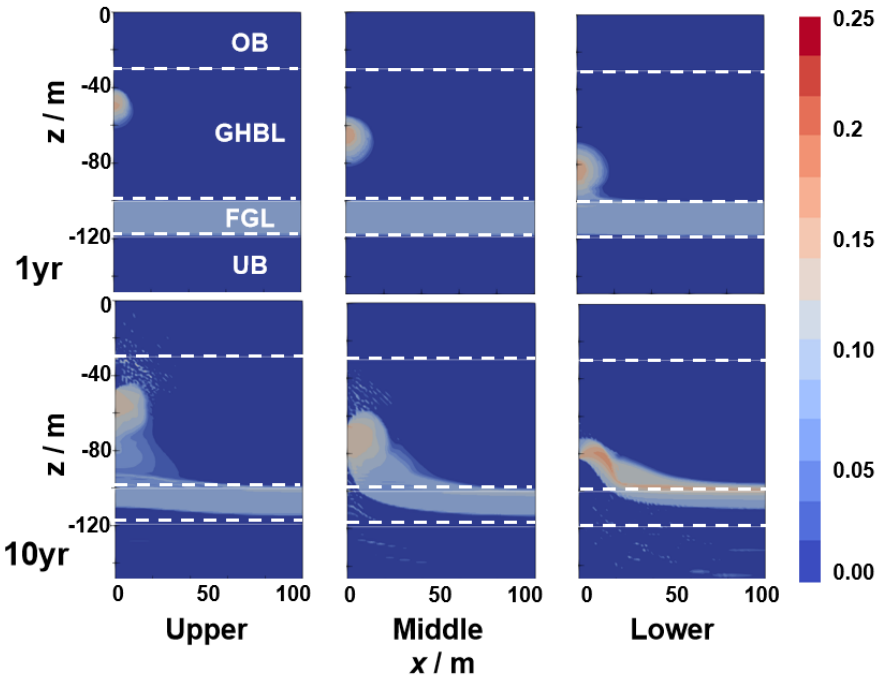

123 (a)

124

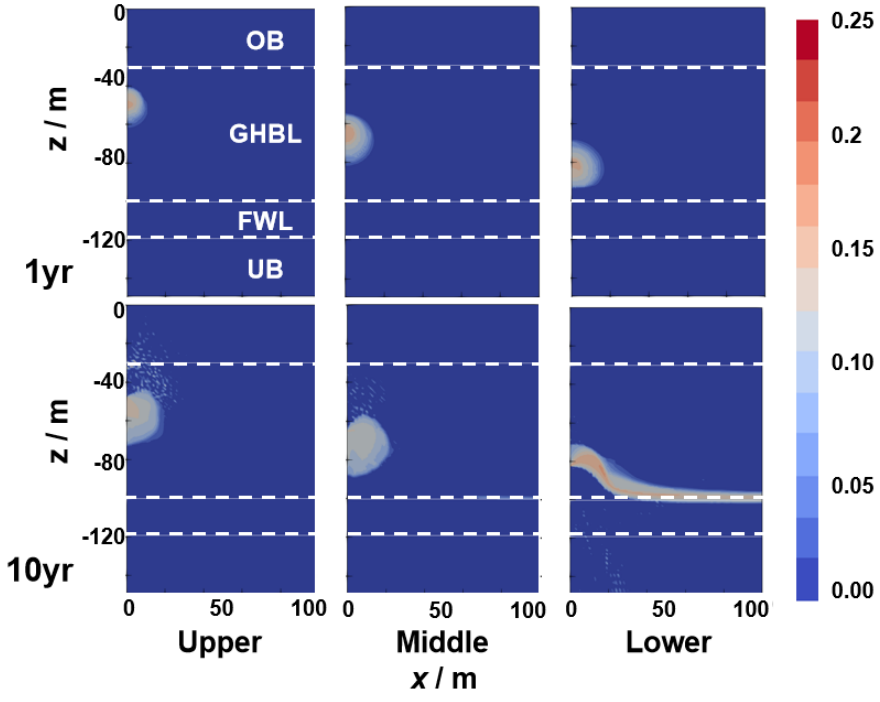

125 (b)

126

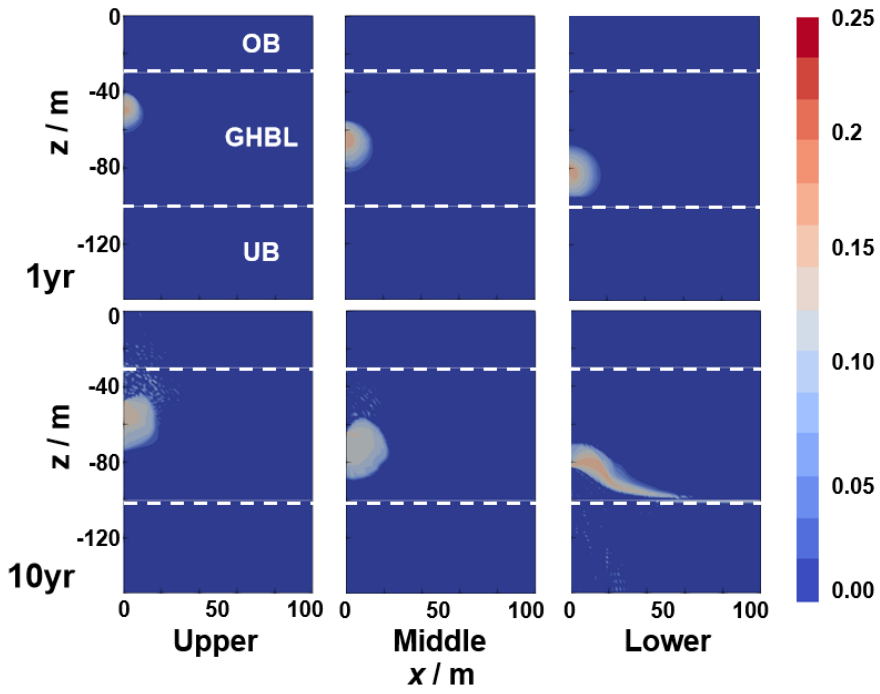

127 (c)

128 Fig. 10 Spatial distribution of gas saturation at 1 year and 10 years under different horizontal well

129 configurations in: (a) Class I; (b) Class II; (c) Class III.

130

131

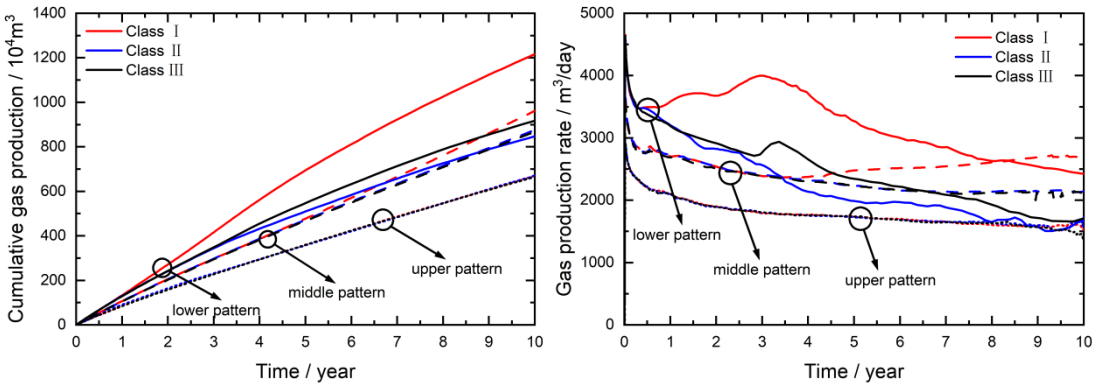

(a) (b)

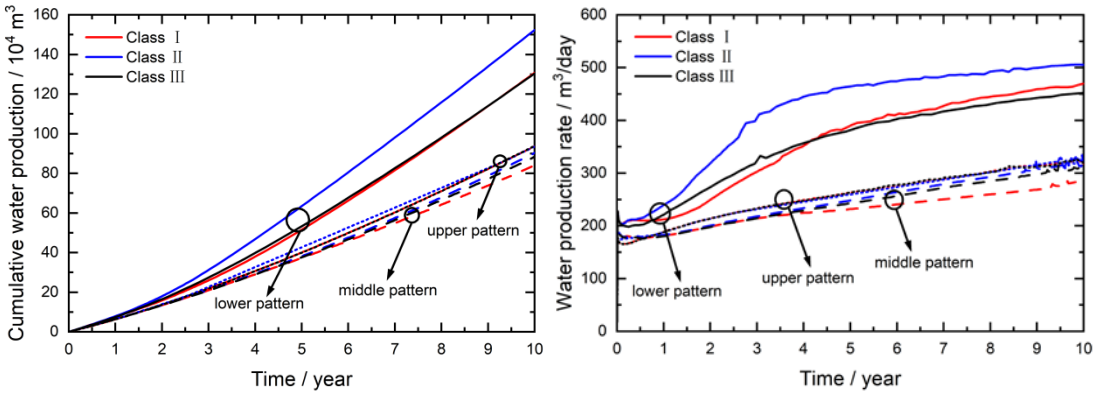

(c) (d)

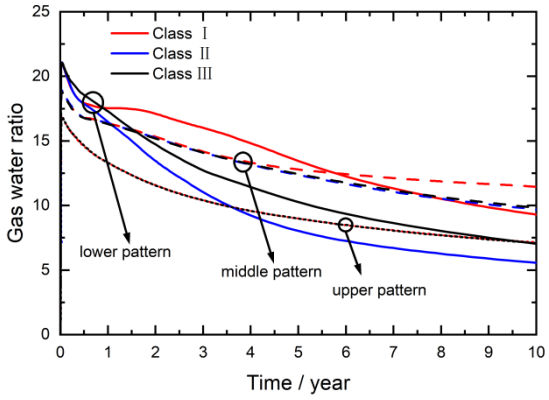

(e)

Fig. 11 Characteristics of gas and water production across different reservoir types and well configurations: (a) cumulative gas production; (b) gas production rate; (c) cumulative water production; (d) water production rate; (e) gas water ratio.

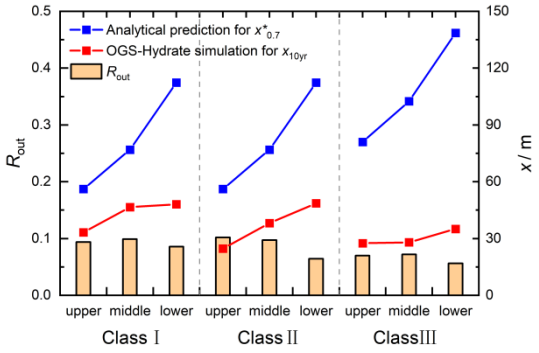

Fig. 12 Comparison of the analytically predicted high-efficiency production zone ($x^*_{0.7}$), simulated 10-year dissociation boundary (x_{10yr}) and recovery factor (R_{out}) for all cases.

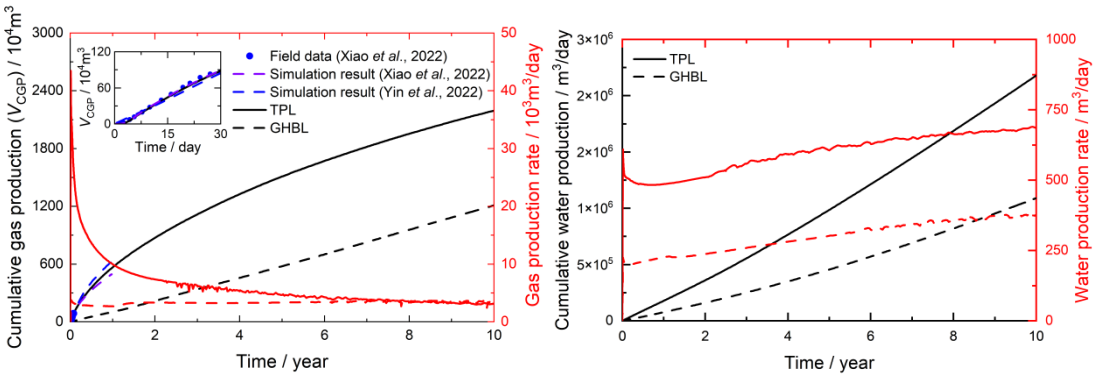

(a) (b)

Fig. 13 Gas and water production characteristics of the second production test in the South China Sea from different well configurations: (a) cumulative gas production and gas production rate; (b) cumulative water production and water production rate.

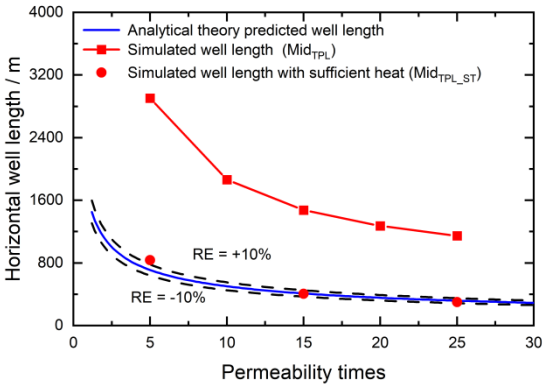

Fig. 14 Predicted minimum horizontal well lengths ($L_{\text{min\_10yr}}$) required to achieve the 10-year commercial production target under different reservoir permeabilities.

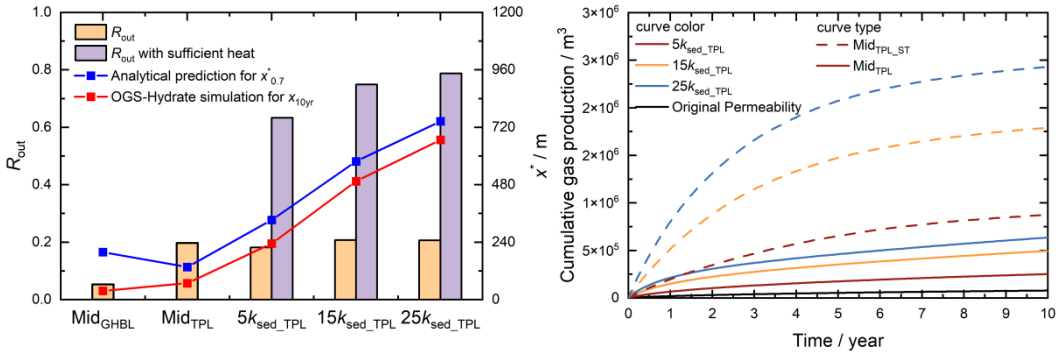

(a) (b)

Fig. 15 Impact of permeability enhancement: (a) recovery factor (R_{out}), the high-efficiency production zone ($x^*_{0.7}$) and the hydrate dissociation boundary after a 10-year simulation (x_{10yr}); (b) cumulative gas production per unit well length.

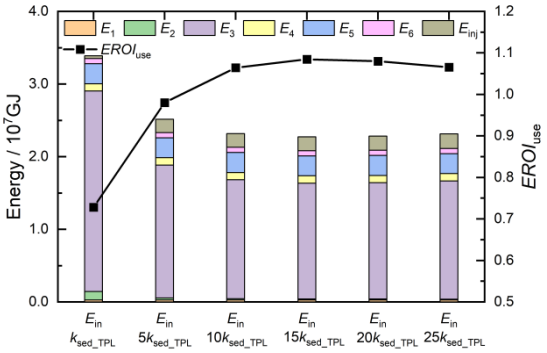

Fig. 16 Evaluation of the energy inputs (E_{in}) and $EROI_{use}$ for commercial production scenarios.

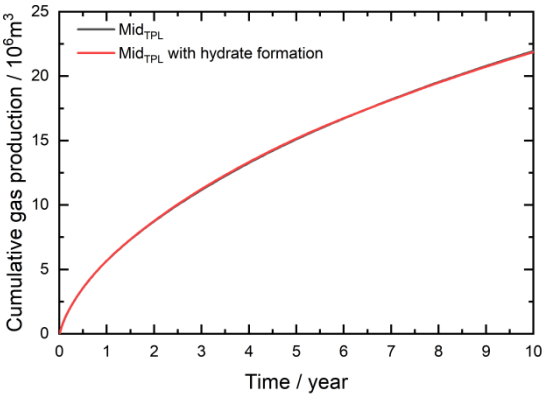

Fig. C-1 Impact assessment of model assumptions and kinetic parameters: effect of secondary hydrate formation.

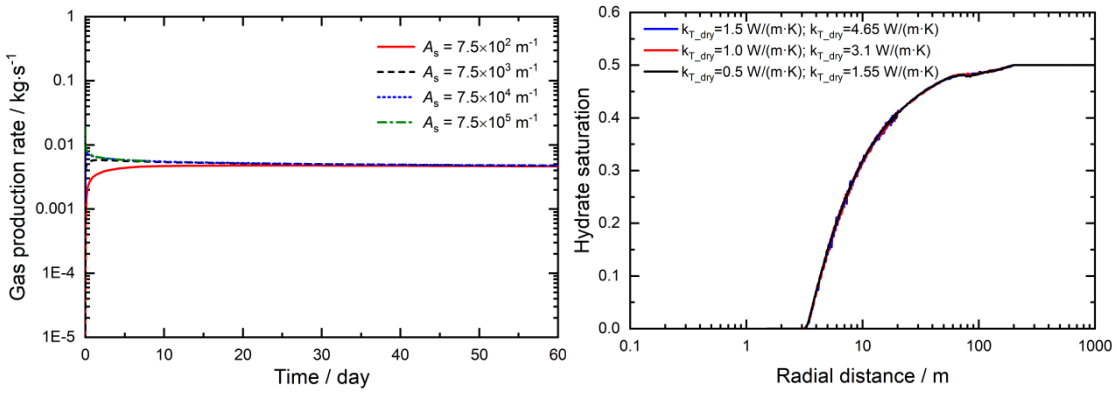

(a) (b)

Fig. C-2 Sensitivity analysis of hydrate dissociation kinetics and thermal properties in IGHCCS2 BP4-Case2: (a) impact of specific surface area of dissociation on gas production rate at day 30; (b) impact of reservoir thermal conductivity on spatial distribution of hydrate saturation at day 30.

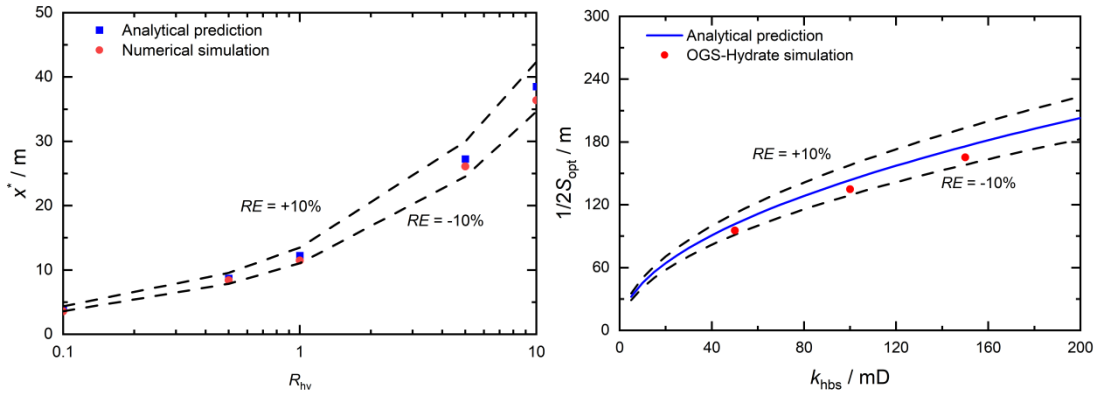

(a) (b)

Fig. C-3 Numerical validation of the applicability of the analytical theory: (a) comparison of gas production range under anisotropic permeability; (b) validation of optimal well spacing under multi-well interference.